Pergamon

Geochimica et Cosmochimica Acta, Vol. 67, No. 18, pp. 3403–3421, 2003

0016-7037/03 $30.00 + .00

doi:10.1016/S0016-7037(03)00127-3

Fluid flow, methane fluxes, carbonate precipitation and biogeochemical turnover in gas hydrate-bearing sediments at Hydrate Ridge, Cascadia Margin: Numerical modeling and mass balances

ROGER LUFF* and KLAUS WALLMANN
GEOMAR Research Center for Marine Geosciences, Wischhofstrasse 1-3 D-24148 Kiel, Germany

(*Received October* 22, 2002; *accepted in revised form February* 6, 2003)

Abstract—A numerical model was applied to investigate and to quantify biogeochemical processes and methane turnover in gas hydrate-bearing surface sediments from a cold vent site situated at Hydrate Ridge, an accretionary structure located in the Cascadia Margin subduction zone. Steady state simulations were carried out to obtain a comprehensive overview on the activity in these sediments which are covered with bacterial mats and are affected by strong fluid flow from below. The model results underline the dominance of advective fluid flow that forces a large inflow of methane from below (869 μmol cm^{-2} a^{-1}) inducing high oxidation rates in the surface layers. Anaerobic methane oxidation is the major process, proceeding at a depth-integrated rate of 870 μmol cm^{-2} a^{-1}. A significant fraction (14%) of bicarbonate produced by anaerobic methane oxidation is removed from the fluids by precipitation of authigenic aragonite and calcite. The total rate of carbonate precipitation (120 μmol cm^{-2} a^{-1}) allows for the build-up of a massive carbonate layer with a thickness of 1 m over a period of 20,000 years. Aragonite is the major carbonate mineral formed by anaerobic methane oxidation if the flow velocity of methane-charge fluids is high enough ($\geq$10 cm a^{-1}) to maintain super-saturation with respect to this highly soluble carbonate phase. It precipitates much faster within the studied surface sediments than previously observed in abiotic laboratory experiments, suggesting microbial catalysis. The investigated station is characterized by high carbon and oxygen turnover rates ($\approx$1000 μmol cm^{-2} a^{-1}) that are well beyond the rates observed at other continental slope sites not affected by fluid venting. This underlines the strong impact of fluid venting on the benthic system, even though the flow velocity of 10 cm a^{-1} derived by the model is relative low compared to fluid flow rates found at other cold vent sites. Non-steady state simulations using measured fluid flow velocities as forcing demonstrate a rapid respond of the sediments within a few days to changes in advective flow. Moreover, they reveal that efficient methane oxidation in these sediments prevents methane outflow into the bottom water over a wide range of fluid flow velocities ($<$80 cm a^{-1}). Only at flow rates exceeding approximately 100 cm a^{-1}, does dissolved methane break through the sediment surface to induce large fluxes of up to 5000 μmol CH$_4$ cm^2 a^{-1} into the overlying bottom water. *Copyright © 2003 Elsevier Ltd*

1. INTRODUCTION

Methane gas hydrates are receiving increasing attention because they are regarded as a major energy source suitable for future exploitation (Kvenvolden, 1993). Moreover, the global climate of the geological past might have been repeatedly effected by greenhouse gases released from hydrates (Dickens et al., 1995; Hesselbo et al., 2000; Jacobsen, 2001). Marine hydrates are common in sediments deposited at polar continental shelves and at the slope and rise of productive continental margins (Kvenvolden, 1988, 1998). Usually, they occur at depths well below the sediment surface because methane is rapidly oxidized by microbial consortia using pore water sulfate as oxidizing agent (Boetius et al., 2000). Nevertheless, near-surface gas hydrates have been discovered at a constantly increasing number of continental margin sites affected by gas and fluid venting over the last years (Sassen et al., 1998, 2001; Egorov et al., 1999; Ginsburg et al., 1999, 1993; Suess et al., 1999). In these areas, methane is rapidly transported to the surface sediments with ascending fluids or gas bubbles so that a strong supply of methane from deep layers compensates for methane oxidation and decomposition. Methane transport from below and the constant dissolution of gas hydrates produce a steady flux of methane to the surface, supporting rich benthic ecosystems based on the anaerobic and aerobic oxidation of methane and dissolved sulfide (Suess et al., 1985; Wallmann et al., 1997; Boetius et al., 2000). The oxidation of the ascending methane by sulfate occurs in narrow zones near the sediment surface, where sulfide and bicarbonate are released into the pore water:

$$CH_4 + SO_4^{2-} \rightarrow HCO_3^- + HS^- + H_2O \qquad (1)$$

The sulfide is transported to the sediment surface where it is further oxidized by aerobic bacteria using oxygen and nitrate as terminal electron acceptors. Bicarbonate released during anaerobic methane oxidation (Eqn. 1) increases the alkalinity and supports the precipitation of authigenic carbonates according to (Berner, 1980):

$$Ca^{2+} + 2HCO_3^- \Leftrightarrow CaCO_3(s) + CO_2 + H_2O \qquad (2)$$

High- and low-magnesium calcite as well as aragonite precipitates are abundant around cold vent sites where methane-rich fluids are present in surface sediments (Kulm et al., 1986; Bohrmann et al., 1998). Carbonate precipitation in these sedi-

---

* Author to whom correspondence should be addressed (rluff@geomar.de).

ments is regarded as a major sink of methane derived carbon and seawater Ca (Han and Suess, 1989) even though precipitation mechanisms and rates are still poorly understood.

The model study presented in this article is based on pore water data obtained at Hydrate Ridge, a segment of the Cascadia convergent margin. The ongoing studies at this site have revealed high and variable rates of fluid venting (Linke et al., 1994; Tryon et al., 1999; Tryon and Brown, 2001), gas venting and out-cropping of gas hydrates (Suess et al., 1999), abundant carbonate precipitates (Bohrmann et al., 1998), and rich benthic ecosystems relying on the oxidation of methane and sulfide (Suess et al., 1999; Boetius et al., 2000; Elvert et al., 2001).

The numerical model C. CANDI (Luff et al., 2000) is applied to simulate the biogeochemical processes in methane-bearing sediments from Hydrate Ridge affected by fluid venting. It is used to determine the:

- main biogeochemical processes occurring in sediments above gas hydrate layers;
- velocity of advective fluid transport through the sediment;
- amount of methane that reaches the upper sediment column and the bottom water;
- calcite/aragonite precipitation rates;
- benthic fluxes of dissolved species between sediment and bottom water;
- response of the system to changes in pore water flow velocities;
- relation between SO_4^{2-} penetration depth and velocity of pore water fluxes.

Our study gives the first quantitative budget of carbon fluxes in hydrate-bearing sediments accounting for methane oxidation, carbonate precipitation and turnover of particulate organic carbon.

2. STUDY AREA

Hydrate Ridge is a part of the north-south striking accretionary complex at the Cascadia margin ~90 km offshore central Oregon, USA (Fig. 1). Tectonic uplift, thrusting and compaction driven by plate convergence are responsible for an advective transport of methane-rich fluids from deep sediments to the surface. Video-surveys and sediment coring with RV SONNE revealed a characteristic zonation pattern of benthic communities around vent sites at Hydrate Ridge (Sahling et al., 2002). At the center of active venting, sediments are covered with thick bacterial mats composed of filamentous sulfide-oxidizing microorganisms (*Beggiatoa* sp.). Underlying sediments contain gas hydrates at shallow depths (Bohrmann et al., 2000), whereas surrounding sediments are inhabited by different clams and bivalves (*Calyptogena pacifica, C. kilmeri, Acharax* sp.) that also rely on methane and sulfide fluxes from below. Pore water studies revealed that the dissolved sulfide contents of surface sediments strongly decline from high concentrations at the center covered with microbial mats (up to 20 mM TH_2S) to low micro-molar levels at the fringes of the vent system (Sahling et al., 2002). In-situ measurements of fluid flow suggest that the highest fluid flow rates of up to 1000 cm a^{-1} occur at the central part of the vent system covered by microbial mats (Tryon and Brown, 2001). The model study presented in this article is based on a sediment core (SO143/55-2) recovered with a TV-guided multi-corer from the center of an active vent site located at the crest of the southern summit (44°34.150N; 125°08.730W). This sediment core was covered with a thick bacterial mat and ended at a massive layer of gas hydrate at a depth of 15 cm. The core was taken during RV SONNE cruise SO143 in July 1999 at a water depth of about 790 m (Fig. 1).

Authigenic carbonate minerals are abundant at Hydrate Ridge. The full suite of carbonate mineralogies including dolomite, proto-dolomite, high magnesium calcite, low magnesium calcite and aragonite have been found at the ridge (Bohrmann et al., 1998; Greinert et al., 2001). The crest of the northern summit is covered with carbonate boulders which pave the seafloor in several layers forming a 20 m thick and 400 m wide structure (Greinert et al., 2001). Randomly distributed single carbonate blocks and yellow-colored carbonate crusts composed of aragonite were observed at the top of the southern summit. The aragonite crusts occur in direct contact with and even inside the gas hydrate fabric (Bohrmann et al., 1998; Greinert et al., 2001). Stable isotope analysis of aragonite samples confirms that these carbonates result from methane oxidation in surface sediments (Greinert et al., 2001). Aragonite can thus be regarded as the characteristic carbonate mineral formed during anaerobic oxidation of methane in hydrate-bearing surface sediments (Bohrmann et al., 1998; Greinert et al., 2001). The investigated sediment core had an average $CaCO_3$ content of 15%wt finely dispersed throughout the whole sediment matrix. At reference stations not affected by fluid venting the carbonate contents were below the detection limit (<1%wt $CaCO_3$). Thus, the carbonate at the studied vent location was entirely produced by authigenic carbonate precipitation processes.

3. SAMPLING AND CHEMICAL ANALYSIS

A multi-corer equipped with a video system was deployed to place the coring device directly in the center of the vent field covered with bacterial mats. Multi-corers are designed to recover undisturbed surface sediments and are therefore well suited to study benthic processes. After recovery, sediment cores were rapidly transferred to the on-board laboratory which was cooled to 4°C to prevent heating. The cores were segmented into cm slices which were given into a squeezer to separate pore waters and solids. Rapid segmentation and squeezing was essential because the methane-loaded pore fluids and the sedimentary gas hydrates started to release large amounts of gaseous methane due to the pressure decrease upon core recovery.

Pore waters were analyzed on-board for dissolved ammonia, nitrate, phosphate, and sulfide using standard photometric procedures (Grasshoff et al., 1983; Gieskes et al., 1991). Total alkalinity was determined by titration (Ivanenkov and Lyakhin, 1978) immediately after pore water separation and pH values were determined in wet sediment samples before squeezing. The remaining pore waters were later analyzed in the shore based laboratory for dissolved sulfate and dissolved elements (Mg, Ca, B, Mn) using ion-chromatography and optical ICP, respectively. Subsamples for dissolved Ca analysis were acidified immediately after squeezing to prevent further $CaCO_3$ precipitation. Total carbon, organic carbon, organic nitrogen

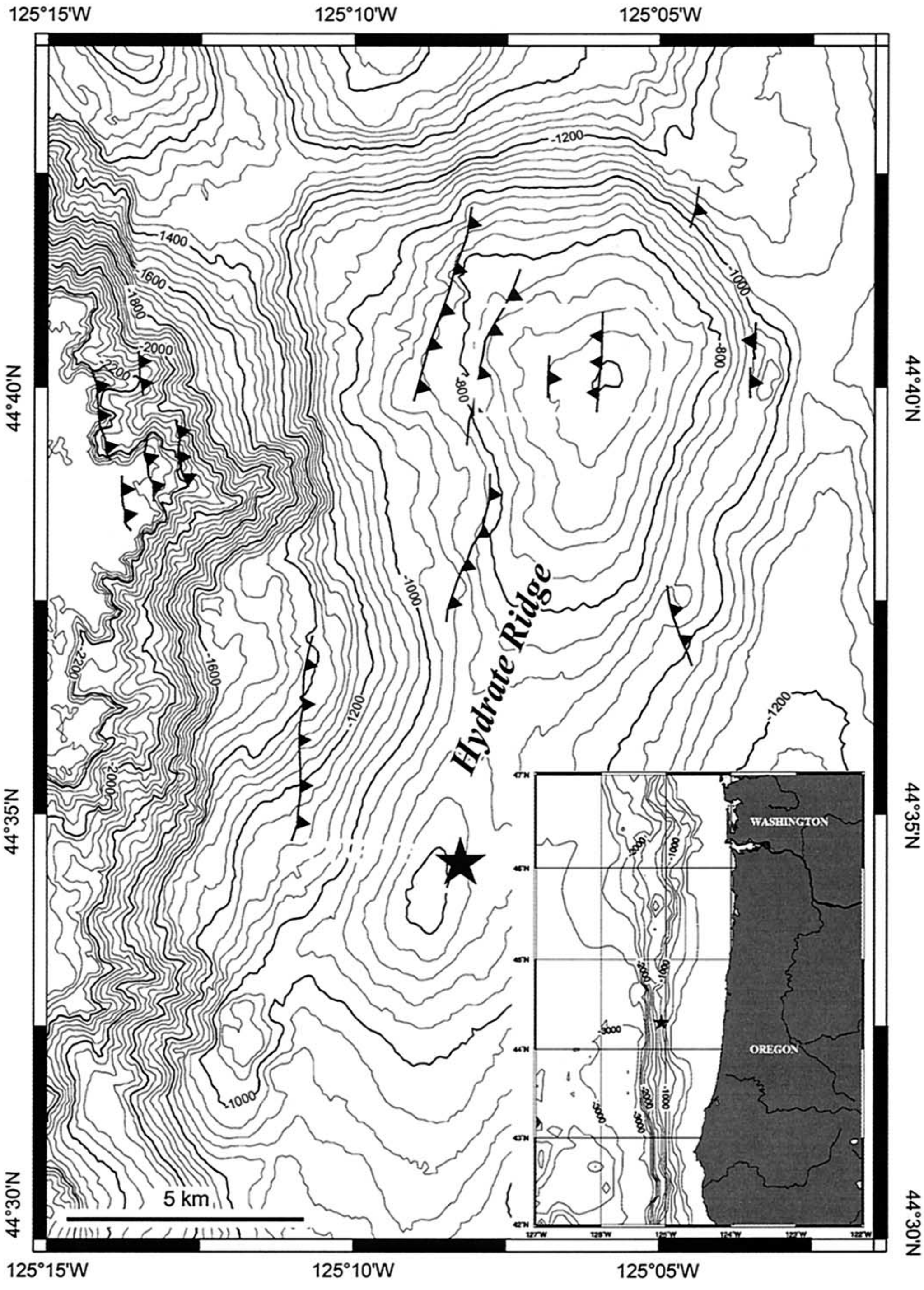

Fig. 1. Location of the study area off Oregon, USA. The investigated station at the southern summit (44°34.150N; 125°08.730W) of Hydrate Ridge situated at a water depth of 790 m has been marked with a star.

and sulfur were determined using an element analyzer. Solid phase concentrations of Fe and Mn were determined after acid digestion using optical ICP. All analytical procedures applied on board of research vessels and in our GEOMAR laboratories are documented in detail at http://www.geomar.de/zd/labs/labore_umwelt/Meth_englisch.html.

4. SET-UP OF THE NUMERICAL MODEL

The numerical model C. CANDI (**C**alcite, **C**arbon **A**nd **N**utrient **D**iagenesis) was applied to simulate the biogeochemical processes in the surface sediments of Hydrate Ridge (see Luff et al., 2000 for a comprehensive model description). The model

Table 1. Summary of constant parameter values used as boundary values for the modelling.

Parameter	Value	Unit
Temperature (Bohrmann et al., 2000)	4.2	°C
Salinity (Bohrmann et al., 2000)	34.30	PSU
Pressure (Bohrmann et al., 2000)	78.0	Atm
Sedimentation rate (Hempel, 1995)	$27.5 \cdot 10^{-3}$	cm a^{-1}
Bioturbation coefficient at the surface (D_b0)	0.01	cm^2 a^{-1}
Depth where D_b is zero	3.0	cm
Porosity at sediment surface	0.80	
Porosity in great sediment depth	0.67	
Porosity depth attenuation coefficient	0.22	
Bioirrigation coefficient	0.0	a^{-1}
Pore water boundary values:		
BW O_2/BS O_2	0/0	mM
BW NO_3^-/BW NO_3^-	0/0	mM
BW SO_4^{2-} (from salinity)/BS SO_4^{2-}	27.8/0	mM
BW Ca (from salinity)/BS Ca	10.1/3.5	mM
BW CH_4/BS CH_4	0/68	mM
BW Mn^{2+}/BS Mn^{2+}	$0/0.2 \cdot 10^{-3}$	mM
BW TPO4/BS TPO4	$0.45 \cdot 10^{-3}/0.15 \cdot 10^{-3}$	mM
BW TNH4/BS TNH4	0.1/0.23	mM
BW CO_2^-/BS CO_2 (from TA, TH2S, see text)	0.3/0.75	mM
BW HCO_3^-/BS HCO_3^- (from TA, TH2S, see text)	2.2/15.6	mM
BW CO_3^{2-}/BS CO_3^{2-} (from TA, TH2S, see text)	0.03/0.2	mM
BW H_2S/BS H_2S (from TA, TH2S, see text)	1.0/4.1	mM
BW HS^-/BS HS^- (from TA, TH2S, see text)	2.5/15.9	mM
Solid species boundary values:		
SS Mn(IV)	0.01	%wt
SS Fe(III)	0.05	%wt

BW indicates concentrations of dissolved species at the upper boundary of the model column, SS are concentrations of solids at the upper boundary, and BS indicates concentrations of dissolved species at the bottom of the sediment column. All boundary values are taken from measurements done in the TECFLUX project if not otherwise noted.

considers the degradation of organic matter separated in 2 different fractions (2-G), the consumption of terminal electron acceptors O_2, NO_3^-, Mn(IV), Fe(III), SO_4^{2-}, methanogenesis, 17 secondary redox reactions including anaerobic methane oxidation, acid-base equilibria, and carbonate dissolution and precipitation processes (Luff et al., 2001). Altogether the distribution of 22 species (O_2, NO_3^-, Mn(IV), Fe(III), SO_4^{2-}, CH_4, TPO4, TNH4, TBOH4, Mn^{2+}, Fe^{2+}, FeS, $C_{org\#1}$, $C_{org\#2}$, H_2S, HS^-, CO_2, CO_3^{2-}, HCO_3^-, Ca^{2+}, calcite, aragonite), solid and solute, in the sediment and the pore water, forced by advection, irrigation, molecular diffusion, bioturbation and chemical/biologic reactions have been described with the model at the cold vents site. The rates of the kinetically controlled redox reactions are formulated following Van Cappellen and Wang (1996) and Boudreau (1996). Dissolution and precipitation rate laws for calcium carbonate (Eqn. 4) were taken from Hales and Emerson (1997). Finally, pH calculations were performed using the advancement approach as outlined in Luff et al. (2001). The model can be used to perform both steady-state as well as non-steady state simulations. Species in the model that consist of more than one compound e.g., TBOH4 = $B(OH)_3 + B(OH)_4^-$ are labeled with a capital T at the beginning using no subscript for the stoichiometric coefficients.

The vertical resolution of the modelling grid was set to 1000 layers (i.e., 0.15 mm thickness of each layer) to resolve the concentration gradients, especially at the surface, and to calculate realistic fluxes between the sediment and the overlying bacterial mat. The complete set of parameters used as boundary values for the biogeochemical description of this site is summarized in Table 1. All parameter values were taken from measurements obtained within the TECFLUX project at Hydrate Ridge, if not otherwise noted. The early diagenetic processes described by the C. CANDI model are mainly driven by the depositional flux of organic matter to the sediment surface. Thus, application of the model to a cold vent site affected by methane venting and covered with a bacterial mat requires modifications to the model code which are described in the following.

Advective pore water flux from below moving upwards through the simulated sediment column was included in the model. The velocity of water flow which is in this case composed of the downward burial component modified by compaction and the upward fluid advection is defined as:

$$u(z) = \frac{(w(\infty) \cdot \varphi(\infty) - u(0) \cdot \varphi(0))}{\varphi(z)} \tag{3}$$

where $u(z)$ and $\varphi(z)$ represent the depth-dependent fluid flow velocity and porosity, while $\varphi(\propto)$ and $w(\propto)$ are porosity and burial velocity of solids at infinite depth. The parameter $u(0)$ gives the surface value of the fluid flow, induced from below and $\varphi(0)$ defines the porosity at the surface.

The advective flux from below also requires a new boundary condition for the solute species at the bottom of the sediment column. The fluid flux from deeper sediments in active margin sediments transports pore waters with specific species concentrations into the simulated sediment column. To take the attributes of the ascending pore fluids into account, the measured concentration at the bottom layer of the sediment were prescribed in the last layer of the model. The concentration of the individual dissolved inorganic carbon and sulfide species (CO_3^{2-}, HCO_3^-, CO_2, HS^- and H_2S) were defined considering the measured total concentrations (TCO2, TH2S) at depth and assuming saturation with respect to calcite. Methane concentration at the bottom boundary were calculated considering equilibrium with gas hydrate (Zatsepina and Buffett, 1997) because the investigated sediment core ended at a solid gas hydrate layer. For the solid species, the bottom boundary was defined as open to consider downward advection evoked by sedimentation.

At the investigated site, a clearly visible bacterial mat covers the sediment surface. The complex processes within this mat are not taken into account in the numerical simulation. The model description ends at the interface between sediment and mat. Therefore, the processes occurring in the mat had to be considered in the definition of the upper boundary values. Concentrations of O_2 and NO_3^- were set to zero as suggested by microelectrode studies (Jorgensen and Revsbech, 1983; Sweerts et al., 1990). Following this approach, other concentration values for the sediment boundary e.g., TPO4, TNH4 TH2S were taken from measurements within the upper sediment layer, not from the bottom water, whereas boundary concentrations of SO_4^{2-}, Ca, and TBOH4 were calculated from bottom water salinity because the concentrations of these major ions are less affected by processes in the mat.

Close investigations of the benthic fauna at Hydrate Ridge showed that surface sediments underlying bacterial mats are almost devoid of eukaryotic organisms larger than 30 μm (Sommer et al., 2002). Thus, bioturbation and bioirrigation do not contribute significantly to the transport of solids and solutes at these sites. The prescribed surface bioturbation coefficient was hence set to the very small value of 0.01 $cm^2\ a^{-1}$ and bioturbation was assumed to vanish completely at a depth of 3 cm using a 2-layer approach (Boudreau, 1996). Bioirrigation - e.g., non local pore water transport generated by benthic fauna - was omitted.

The calculation of pH values and saturation states with respect to different carbonate minerals was performed as described in Luff et al. (2001). The three dissolved inorganic carbon species CO_2, HCO_3^-, CO_3^{2-} and the two dissolved sulfide species, H_2S and HS^-, were allowed to equilibrate with H^+ according to the acid dissociation constant of CO_2 and H_2S (Millero, 1995) and were transported individually along their own concentration gradients. The pH values were calculated considering the proton turnover by redox reactions as well as POC degradation processes and the buffering through H_2S, HS^-, CO_2, CO_3^{2-}, HCO_3^-, $B(OH)_3$, and $B(OH)_4^-$.

The precipitation of both aragonite and low-magnesium-calcite are considered in the model applying solubility products according to Millero (1995). The precipitation rates (R_{PPT}) of both carbonate minerals were assumed to depend linearly on the saturation state:

$$R_{PPT} = k_{PPT} \cdot \left(\frac{[Ca^{2+}] \cdot [CO_3^{2-}]}{K_{SP}} - 1 \right)^n \qquad (4)$$

where k_{PPT} is the kinetic constant either for aragonite or calcite, K_{SP} is the thermodynamic equilibrium constant defining aragonite or calcite solubility, $[Ca^{2+}]$ is the prevailing concentration of dissolved calcium, and $[CO_3^{2-}]$ gives the concentration of dissolved carbonate anions. Most previous workers used a similar approach but allowed for a non-linear dependence on saturation state applying different exponents (n) between 0.4 and 2.8 (Burton and Walter, 1987; Zhong and Mucci, 1993). We use a linear dependence ($n = 1$) because the available experimental data for carbonate precipitation from seawater do not consistently suggest a particular reaction order with respect to saturation state.

In the model, dissolution and precipitation are controlled both by thermodynamic and kinetic constraints. Carbonate minerals are allowed to precipitate only if the ion concentration product $[Ca^{2+}] \cdot [CO_3^{2-}]$ is higher than the corresponding solubility product K_{SP} whereas lower ion concentrations induce dissolution (Eqn. 4). Applying Oswald's rule, it is assumed that the kinetic constant for the precipitation of the less stable mineral (aragonite) is an order of magnitude higher than the corresponding constant for the more stable $CaCO_3$ polymorph (calcite). With this formulation, aragonite is precipitated preferentially in a sedimentary environment where carbonate alkalinity is constantly produced by anaerobic methane oxidation as previously proposed by Given and Wilkenson (1985) and suggested by field observations at Hydrate Ridge (Bohrmann et al., 1998; Greinert et al., 2001). When the less stable aragonite dissolves because the production of carbonate alkalinity falls below a critical value, it is re-precipitated as calcite as long as the solution is over saturated with respect to calcite.

The model simulates the turnover of dissolved methane, whereas bubble transport is not considered because video observations showed that the sampled site is not affected by active gas venting. Moreover, formation of gas hydrates in the sediment column is neglected because no gas hydrate was observed within the investigated sediment section. The occurrence of gas hydrates at the base of the model column is taken into account by using the methane concentration in equilibrium with gas hydrates at ambient pressure and temperature conditions as the bottom boundary condition.

5. RESULTS AND DISCUSSION

Critical values of kinetic constants and the unknown flow velocity were determined by fitting the model to the available biogeochemical data set assuming steady state conditions (section 5.1). Subsequent non-steady state simulations (section 5.2) showed that the solute species follow the forcing so quickly, mainly influenced by the advective flow, that each set of measurements of the solutes can be assumed to be in steady state. Additional simulations were performed to explore the controls on carbonate precipitation at the investigated site (section 5.3). The turnover within the overlying bacterial mat was determined using a mass balance approach (section 5.4) and the change in sulfate penetration depth as a function of upward fluid flow has been investigated in section 5.5.

5.1. Steady State Approach

The comparison between data determined in core 55-2 (listed in the Appendix and represented as stars in Fig. 2a and 2b where available) and simulated steady state profiles (solid

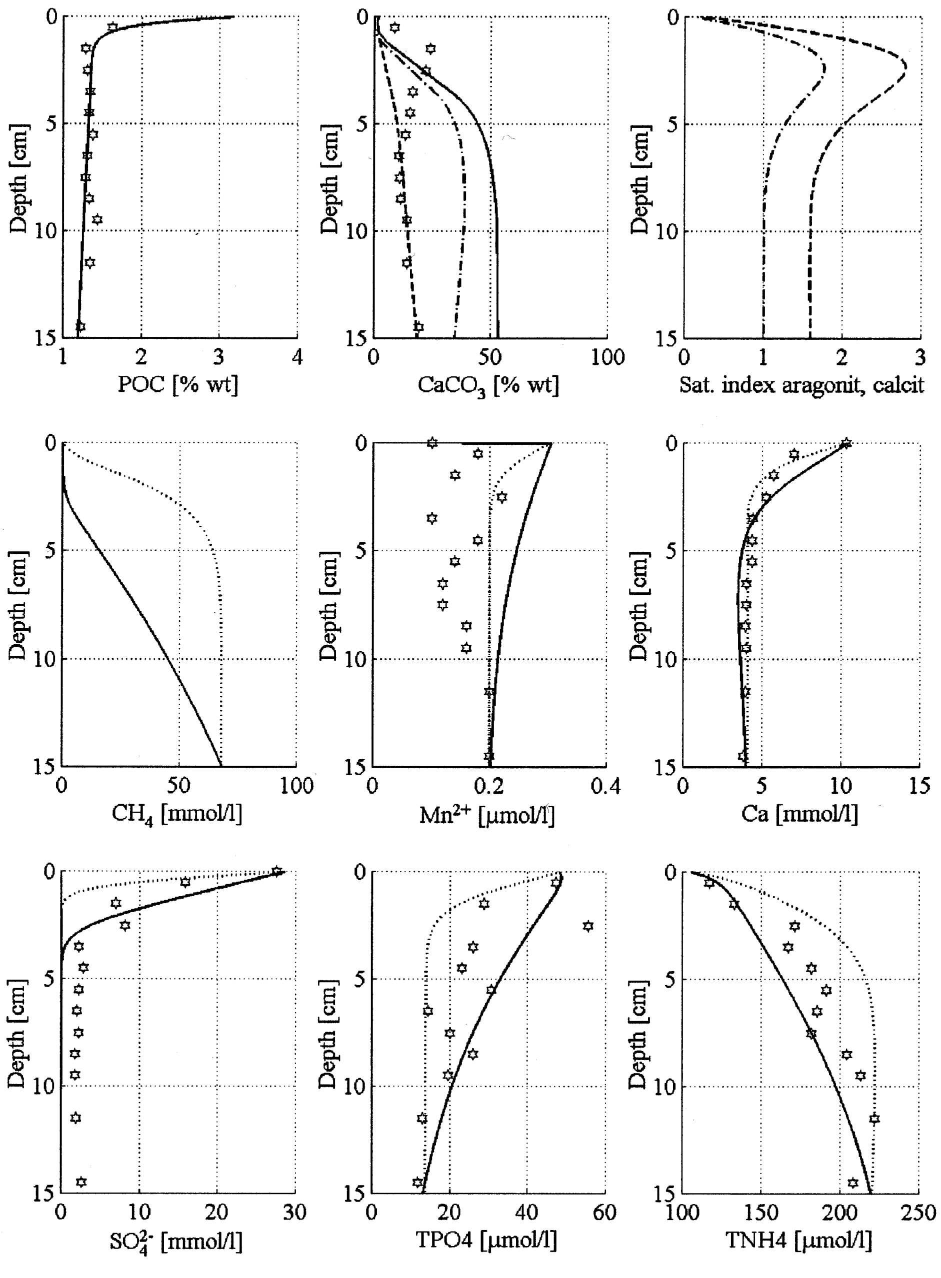

Fig. 2. (a) Simulated and measured concentration profiles. First row: concentration of particular organic matter (POC), calcite (broken line), aragonite (dash-dotted line) and total $CaCO_3$ (solid line), saturation index of calcite (broken line) and aragonite (dash-dotted line). Second row: concentrations of dissolved methane (CH_4), manganese (Mn^{2+}) and calcium (Ca). Third row: concentrations of sulfate (SO_4^{2-}), phosphate (TPO4) and ammonia (TNH4). Simulated steady state profiles are plotted as solid lines whereas measured concentrations are plotted as stars, where available. The dotted lines in the two lower rows represent the concentrations of species as calculated at the end of the non-steady state simulation.

lines) demonstrates that the model can be used to simulate the biogeochemical situation at the investigated station. The concentration profiles of particulate organic carbon (POC), dissolved calcium (Ca), manganese (Mn^{2+}), phosphate (TPO4), ammonia (TNH4), sulfide (TH2S) and total alkalinity are well reproduced by the model. Significant deviations are observed only for the carbonate contents of the solid phase ($CaCO_3$), the sedimentary pH and dissolved sulfate (SO_4^{2-}) values. The latter two differences are caused by sampling artifacts. During sampling and pH measurement the sediment is subject to intense degassing of methane and CO_2 due to the pressure release upon core retrieval. The CO_2 loss induces a strong increase in pH so that the measured values are much higher than the in-situ values simulated in the model. Sulfide oxidation induced by the penetration of oxygen into anoxic samples is probably responsible for the non-zero sulfate values below 4 cm sediment depth. The mismatch between measured and simulated $CaCO_3$ contents is not surprising considering that the measured data

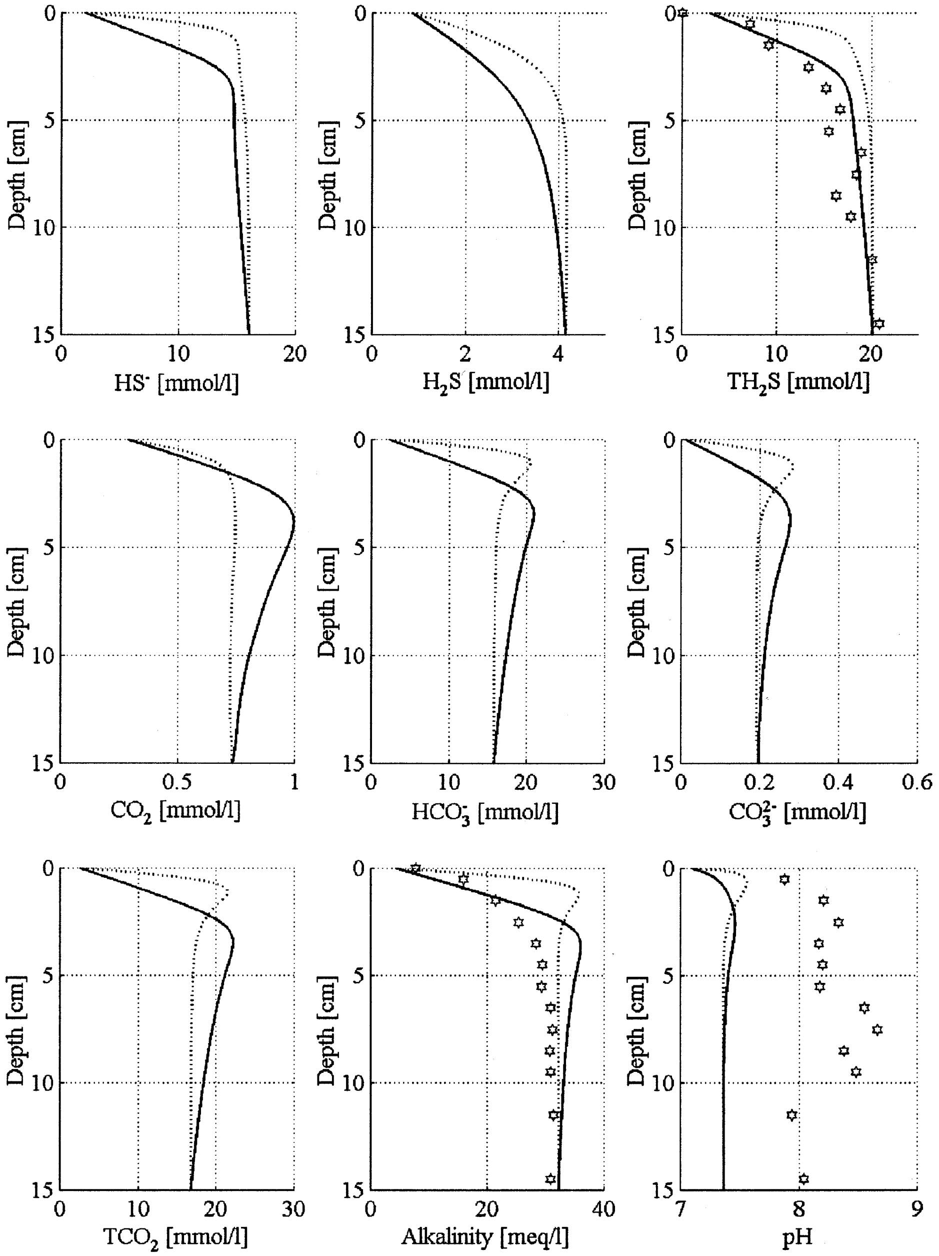

Fig. 2. (b) Simulated and measured concentration profiles. Concentration profiles of HS^-, H_2S, TH2S = HS^- + H_2S, CO_2, HCO_3^-, CO_3^{2-}, TCO2=CO_2 + HCO_3^- + CO_3^2, total alkalinity (TA) and pH from steady state simulations are plotted as solid lines whereas the measured concentrations are plotted as stars, where available. The dotted lines represent species concentrations as calculated at the end on the non-steady state simulation.

reflect the dynamic history of fluid venting and authigenic mineral formation over the last millennium whereas the model curve is determined by current (constant) turnover rates.

The carbon flux to the surface of the model column reflects both the pelagic export production and the turnover of POC in the overlying bacterial mat whereas the POC turnover in the simulated sediment represents the net effect of heterotrophic POC degradation and chemoautotrophic POC production during anaerobic methane oxidation. The bulk of fresh marine POC is highly reactive and is thus degraded at the sediment surface or in the bacterial mat leaving little or almost no trace in the solids and pore fluids of the underlying sediment (Luff et al., 2000). Considering that the studied sediment is characterized by very low rates of bioturbation, the degradation processes are even more focused to the surface so that the highly reactive POC fraction can be ignored in the sediment. The POC flux was assumed to be composed of a moderately labile and a refractory fraction and the fluxes and kinetic constants were set to values satisfying the observed POC, phosphate and ammonia profiles (Table 2).

The major parameters that can be determined with the numerical model are the fluid flow rate, the kinetic constants for

Table 2. Summary of parameter values determined by fitting the results of the steady state simulations to the data.

Parameter	Value	Unit
Kinetic constant of the labile fraction of POM	0.2	a^{-1}
Kinetic constant of the refractory fraction of POM	$3.0 \cdot 10^{-4}$	a^{-1}
Flux of labile fraction POM to the sediment	55	μmol cm^{-2} a^{-1}
Flux of refractory fraction POM to the sediment	26	μmol cm^{-2} a^{-1}
Calcium carbonate flux to the sediment	2	μmol cm^{-2} a^{-1}
Kinetic constant of aragonite dissolution	5	a^{-1}
Kinetic constant of calcite precipitation	10	mmol cm^{-3} a^{-1}
Kinetic constant of aragonite precipitation	100	mmol cm^{-3} a^{-1}
Kinetic constant for anaerobic methane oxidation	100	cm^3 $mmol^{-1}$ a^{-1}
Surface value of pore water vent flow from below	10	cm a^{-1}

anaerobic methane oxidation and the carbonate precipitation rates. They were constrained using the measured sulfate, sulfide, calcium and alkalinity profiles. Due to the strong coupling, variation of one model parameter value affects also several others. For example, enhanced fluid flow rates increase the gradients of all solutes within the surface sediment because of the accelerated upward advection and by increased influx of methane into the simulated column from below (see Fig. 2a and 2b, dotted lines). High values for the rate constant of anaerobic methane oxidation by sulfate reduction produce strong maxima in dissolved sulfide, alkalinity carbonates and pH within the surface sediment whereas low values for this constant strongly increase the sulfate penetration depth. Variation of the kinetic constant for carbonate precipitation (k_{PPT}, Eqn. 4) affects the carbonate, Ca and alkalinity distributions. The results of further parameter variation are discussed in detail in sections 5.2, 5.3 and 5.5. Repeated model runs showed that the best steady state fit to the data was obtained applying the combination of parameter values listed in Table 2. The resulting advective pore water flux of 10 cm a^{-1} is orders of magnitude lower than the extreme value of up to 1065 m a^{-1} reported by Linke et al. (1994) for Hydrate Ridge, but falls into the range of fluxes (0 - 1000 cm a^{-1}) measured by Tryon and Brown (2001) at bacterial mat sites situated on the northern and southern summits of Hydrate Ridge. The kinetic constant k_{CH4SO4} is applied to define the rate of anaerobic methane oxidation assuming bimolecular kinetics with respect to methane and sulfate concentrations:

$$R_{CH_4SO_4} = k_{CH_4SO_4} \cdot [CH_4] \cdot [SO_4^{2-}] \tag{5}$$

This simple rate law is usually applied in early diagenetic modeling (Boudreau, 1996; Van Cappellen and Wang, 1996) even though the controls on anaerobic methane oxidation are poorly understood and might involve other environmental factors such as pH and alkalinity. The value derived from the modeling (k_{CH4SO4} = 100 cm^3 $mmol^{-1}$ a^{-1}) falls into the range of values found in other sedimentary environments (0 - 10 000 cm^3 $mmol^{-1}$ a^{-1}, Iversen and Jørgensen, 1985; Van Cappellen and Wang, 1996).

The kinetic constants for carbonate precipitation, here calculated in rather unusual units (mmol $CaCO_3$ precipitated per cm^3 of wet sediment per year, Table 2), were converted into the dimensions commonly used in experimental studies (μmol carbonate precipitated per m^2 of available seed surface area per hour) assuming an available surface area of $\approx$1 m^2 (g $CaCO_3)^{-1}$ (Burton and Walter, 1987) and applying the prevailing concentrations of calcite and aragonite in the simulated surface sediment ($\approx$20%wt at a dry bulk density of $\approx$0.5 g cm^{-3} corresponding to $\approx$0.1 g $CaCO_3$ cm^{-3} or 0.1 m^2 $CaCO_3$ surface area per cm^3 of wet sediment). The resulting value for the kinetic constant of calcite precipitation (11 μmol m^{-2} h^{-1}) falls into the range of data determined previously in the experimental precipitation of calcite from phosphate-free seawater at 5 to 25°C (1 - 14 μmol m^{-2} h^{-1}; Burton and Walter, 1987; Zhong and Mucci, 1993) whereas the kinetic constant for aragonite precipitation (114 μmol m^{-2} h^{-1}) is higher than the experimental values (22 - 41 μmol m^{-2} h^{-1}, Burton and Walter, 1987).

The rate-depth profiles resulting from the steady state calculations (Fig. 3) allow for a further in-depth interpretation of the biogeochemical processes and their vertical zonation. To present the main processes in each layer the rates are normalized such that the sum of all rates occurring in each layer represents 100%. Starting from the top of the sediment, organic matter degradation using sulfate as terminal electron acceptor (RSO_4) is the main process because no other oxidizing agent (e.g., O_2, NO_3^-) is available in this sediment below the bacterial mat. The low pH at the sediment surface is responsible for dissolution of sedimentary calcite (RCALDIS) in the upper centimeter. Below the first centimeter the high concentration of alkalinity (Fig. 2b) induces precipitation of carbonates. Both aragonite (RARAPPT) and calcite (RCALPPT) are precipitated in the upper 10 cm of the simulated column. Anaerobic methane oxidation (RCH_4SO_4), the dominant process observed at this station, takes place in the upper 5 cm of the sediment column. The turnover rate of this reaction is tremendously high, all methane that reaches the surface sediment from below is oxidized in this layer. Below this highly reactive layer, the turnover is moderate and dominated by methanogenesis as well as carbonate precipitation and dissolution processes. More specifically, continued organic matter degradation in the absence of sulfate releases methane to the pore water (RCH_4), aragonite is dissolved (RARADIS) and re-precipitated as calcite (RCALPPT) below 10 cm depth.

The vertically integrated turnover rates (Table 3) demonstrate, that the biogeochemical turnover at this sites is clearly dominated by anaerobic methane oxidation using sulfate as terminal electron acceptor. The depth integrated steady state rate of this process (925 μmol cm^{-2} a^{-1}) is lower than the sulfate reduction rate previously measured at Hydrate Ridge (5110 μmol cm^{-2} a^{-1}; Boetius et al., 2000) and the mean value of the non-steady state simulation (2637±1250 μmol cm^{-2} a^{-1}; see next section) suggesting that the steady state simulation may be regarded as a minimum estimate of the reaction rates at Hydrate Ridge. Sulfate reduction rates determined at

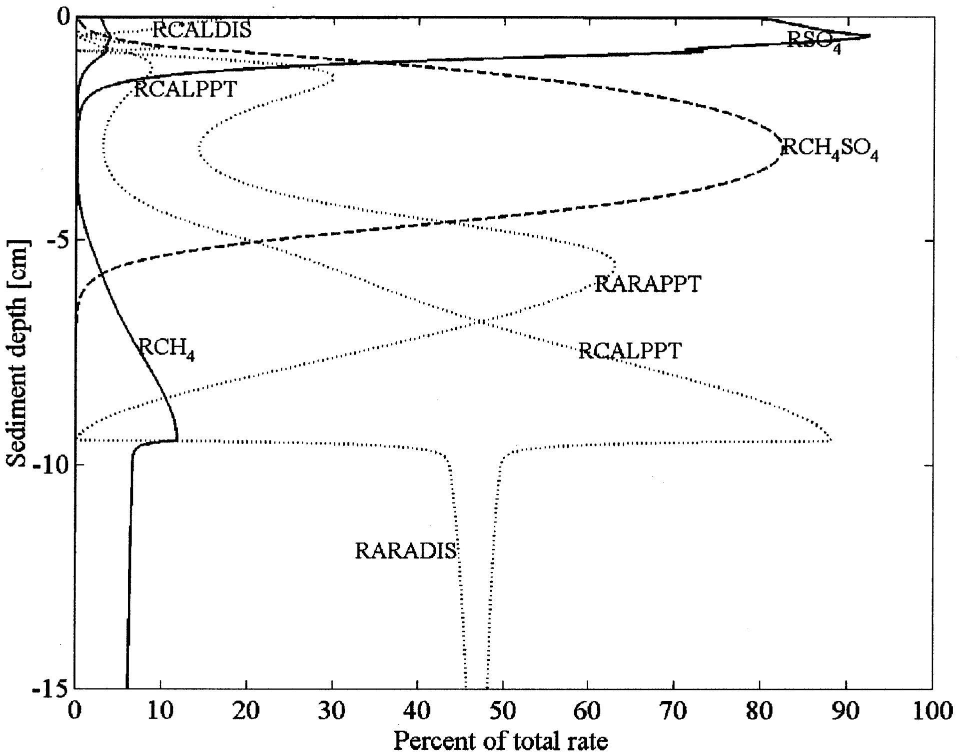

Fig. 3. Relative rate depth profiles of the simulated biogeochemical processes at station 55-2. Solid lines represent primary redox rates, broken lines represent secondary redox rates and dotted lines represent dissolution and precipitation rates. The corresponding processes and the depth integrated values of the presented rates are summarized in Table 3.

other cold vent sites situated in the active subduction zones of the eastern Aleutian trench (1900 μmol cm^{-2} a^{-1}; Wallmann et al., 1997) and the Mediterranean Ridge (100 - 1000 μmol cm^{-2} a^{-1} R. Haese, pers. comm.) are close to the net rate values derived from the steady state simulation suggesting that depth-integrated sulfate reduction rates on the order of 1000 μmol cm^{-2} a^{-1} are a common feature at cold vent sites where methane-bearing fluids are transported to the surface.

The other major reaction at Hydrate Ridge is carbonate precipitation with a depth-integrated net rate of 120 μmol $CaCO_3$ cm^{-2} a^{-1}. This rate can be used to constrain the period of time needed to build the massive carbonate deposits found mainly at the northern summit but also at the southern summit of Hydrate Ridge. Neglecting the effects of carbonate precipitation on sediment permeability and fluid flow, the rate derived in the steady state simulation implies that a massive layer of pure $CaCO_3$ with a thickness of 1 m (corresponding to 260 g $CaCO_3$ cm^{-2} or 2.6 mol $CaCO_3$ cm^{-2}) can be precipitated within about 20,000 yr. Thus, approximately 400,000 yr would have been passed in forming the 20 m thick carbonate layer covering the northern summit of Hydrate Ridge (Greinert et al., 2001) assuming present rates of venting and carbonate precipitation.

Table 3. Depth-integrated rates of primary redox reactions and secondary redox reactions that dominate the system at the investigated station in μmol cm^{-2} a^{-1}.

Name	Type	Description	Depth integrated rate (steady state)	Mean depth integrated rate (non-steady state)
RSO_4	P	oxidation of POM using sulfate	53	48 ± 3.4
RCH_4	P	methanogenesis of POM	5.2	10 ± 3.4
RCH_4SO_4	S	methane oxidation by sulfate	925	2637 ± 1250
RCALPPT	F	precipitation of calcite	39	34 ± 2.7
RARAPPT	F	precipitation of aragonite	89	53 ± 18.2
RCALDIS	F	dissolution of calcite	4.4	1.4 ± 1.2
RARADIS	F	dissolution of aragonite	8.1	5.5 ± 5.9

Values are calculated for the steady state run with a prescribed pore water velocity of 10 cm a^{-1} and for the non-steady state simulation with a flow rate of 125 ± 60 cm a^{-1}. Mean values and associated standard deviations are derived from the depth-integrated rates calculated for each individual day of the non-steady state simulation period (44 d). Reaction types are denoted with P (primary redox reaction), S (secondary redox reaction), and F (dissolution or precipitation reaction). Vertical rate depth profiles are shown in Figure 3.

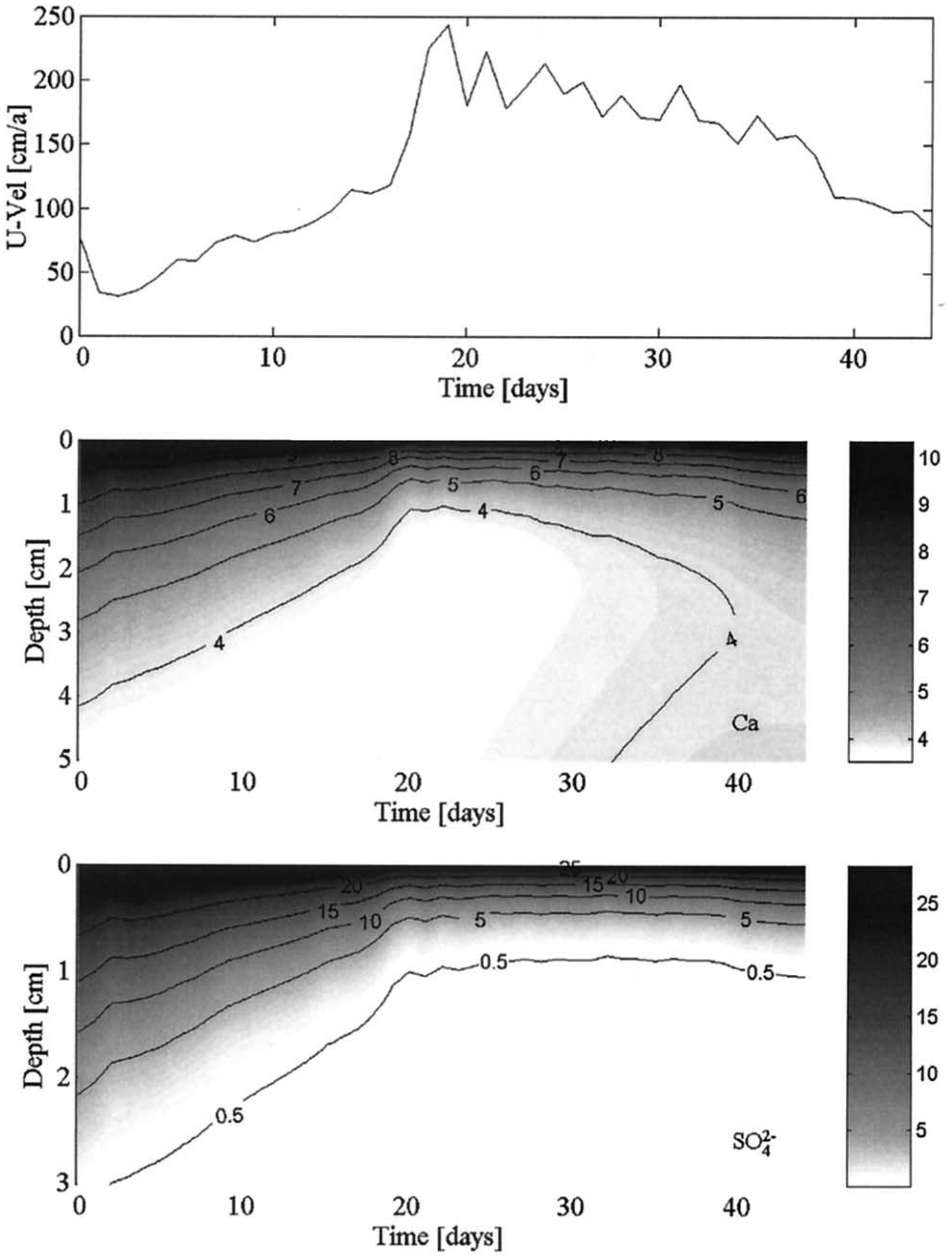

Fig. 4. Effect of variable fluid flow on the distribution of dissolved calcium and sulfate in surface sediments. Top: Vertical water fluxes at the sediment surface [cm a^{-1}] used as forcing for the non-steady state simulation over a period of 44 d to determine the response of the sediment. The fluxes measured by Tryon and Brown (2001) were interpolated to daily values. Middle and bottom: Ca and SO_4^{2-} concentrations (in mM) calculated in the non-steady state simulation in the upper 5 and 3 cm of the sediment, respectively.

5.2. Non-Steady State Simulations

Time-dependent water fluxes measured at Hydrate Ridge with a flow meter deployed on top of a bacterial mat over a period of 6 weeks (Tryon and Brown, 2001) were used as forcing function for a non-steady state simulation applying the parameters derived from the previous steady state simulation. Fluid flow meters were deployed on the northern and southern summit of Hydrate Ridge. The outflow of the sediment recorded on the southern summit was unusually high, much higher than typically found on mat sites (Tryon, pers. com.). Thus, we chose the more typical data set measured on the northern summit for the non-steady state simulation applying a daily interpolation to the original data (Fig. 4, top). The steady state concentration distributions of all simulated species shown in Figure 2a and 2b were used as starting values for this non-steady state simulation.

To demonstrate the effect of the pore water flow, we present the temporal and spatial distribution of dissolved Ca (Fig. 4, middle panel) and SO_4^{2-} (Fig. 4, bottom panel). Both species are consumed in the sediment, but they react differently to changes in flow velocity. The increase in fluid flux over the first 15 d of the simulation steepened the concentration gradients of both species in the upper sediment (Fig. 4). The 4 mM Ca contour line was shifted upwards to about 2.5 cm depth while the sulfate penetration depth, as marked by the 0.5 mM contour line, decreased significantly. The strong increase in flow between day 15 and 20 induced a further steepening of concentration gradients. The 4 mM contour line of Ca was pushed up to about 1.5 cm sediment depth whereas the sulfate penetration depth was further diminished to about 1 cm depth. After day 20 the fluid flow velocity slowly decreased and the Ca gradients were restored, while the sulfate penetration depth remained relatively constant. The high amount of methane still present in the surface sediments slowed the response of the sulfate concentration because sulfate levels could only recover after methane oxidation in the upper sediment column was completed. In contrast, the Ca concentration followed the forcing of the flow velocity directly because Ca removal by carbonate precipitation proceeds at a much lower rate than anaerobic methane oxidation.

The strong effects of fluid flow on pore water distributions can also be observed in the concentration profiles of the other species shown in Figure 2a and 2b where the dotted lines represent the concentration profiles at the end of the non-steady state simulation. The increase in advection velocity induces stronger gradients near the sediment surface for all solutes while the concentration profiles of the solids are not affected on the short time scales of this simulation. In conclusion, the non-steady state simulation clearly depicts the strong influence of the upward flow velocity on the species distributions of the pore water. Within a few days the species concentrations and the gradients in the sediment change significantly only forced by the fluid flow.

The fluxes of solutes between sediment and overlying bacterial mat are also strongly influenced by the time-dependent velocity of fluid flow. The benthic methane fluxes calculated with the model demonstrate the non-linear interactions between the physical forcing and the biogeochemical reactions occurring in the sediments (Fig. 5). When the flux velocities are low, the methane input from below can be balanced by anoxic methane oxidation. Thus, the increase in flux during the first 10 d of the non-steady state simulation (Fig. 4, top) has little effect on the benthic methane flux. It remains at a low and almost constant value of about 0.3 μmol cm^{-2} a^{-1}. The additional methane that reaches the surface sediments is oxidized completely by microbial consortia. The increase in upwards advection also hinders the mass transport of sulfate from the bottom water. As a consequence, the oxidation takes place higher in the sediment so that the distance between reaction horizon and overlying bottom water is shortened, gradients are steeper (Fig. 4, bottom) and the diffusive sulfate flux into the sediment increases (Fig. 5) to balance the enhanced methane influx. At even higher rates of advective methane inflow from below, the diffusive sulfate flux can not compensate for the enhanced methane flow so that methane breaks through the surface inducing large methane fluxes (up to 5000 μmol cm^{-2} a^{-1}) into the overlying bacterial mat. The flux decreases rapidly after day 30 of the simulation when the flow velocity falls below the critical threshold value of about 100 cm a^{-1} while the SO_4^{2-} flux stays at a high level because the anaerobic bacterial consortia consume sulfate continuously until the methane pool in the surface layer is completely oxidized. The fluxes of dissolved sulfide, and carbon species are also strongly affected by the flow velocity (Fig. 5 note the logarithmic scale used for dissolved carbon species). They increase significantly over the first 20 d of the simulation as a result of the increase of methane oxidation. Thus, the flux of HCO_3^- is enhanced from 1200 μmol cm^{-2} a^{-1} to more than 6600 μmol cm^{-2} a^{-1} over this period. Because of the buffer capacity of the sediment a time lack of about 10 d between forcing and reaction of the species involved in anoxic methane oxidation can be observed in Figure 5. At day 20 of the simulation, the pore water velocity reaches its maximum value of 240 cm a^{-1}, while the methane outflow from the sediment and the sulfate flux into the sediment reach their maxima at day 30. This shift is also observed for HS^- whereas the inorganic carbonate species and H_2S follow the forcing directly.

Depth-integrated rates were calculated for each day of the non-steady state simulation. The values of these rates averaged over the whole model period (44 d) are listed in Table 3. The mean value of the vertical pore water velocity during the non-steady state simulation was 125±60 cm a^{-1}. Because flow velocity is such a crucial variable, the average rates and their standard deviations can be used to describe the dynamics of the system. The comparison with the vertically integrated rates of the steady state simulation shows that the anaerobic methane oxidation is strongly affected by changes in the pore water velocity. The depth-integrated rate increases by a factor of 2.8 to a value of 2637 μmol cm^{-2} a^{-1} with a maximum value of 4070 μmol cm^{-2} a^{-1}. The reduction of the sulfate penetration depth during this simulation evokes a shift from organic matter degradation via sulfate reduction to a larger portion of methanogenesis. Moreover, the precipitation rates of carbonates are reduced when pore water flow is higher because the precipitation zone is shifted towards the surface where fluids tend to be undersaturated due to the prescribed upper boundary values. A similar effect probably occurs in the natural system because aerobic sulfide oxidation within the overlying bacterial mat leads to a massive release of protons (Eqn. 6).

5.3. Controls on Carbonate Precipitation in Anoxic Sediments

The controls on carbonate precipitation in anoxic surface sediments affected by anaerobic methane oxidation are controversial (Wilkenson, 1989). The rates may be affected by the delivery of Ca^{2+} ions from the overlying seawater, by the rate of methane oxidation that produces alkalinity, and by reactions occurring at the mineral surface (Berner, 1980; Raiswell, 1988; Wilkenson, 1989). Hence, additional scenarios based on the parameter definition of the steady state simulation (Fig. 2a and 2b) were performed to explore the controls on carbonate precipitation at the investigated site (Table 4, Fig. 6).

In scenario A, the same parameter values were used as in the previous steady state simulation. The length of the model column has been increased from 15 cm to 40 cm to allow for a

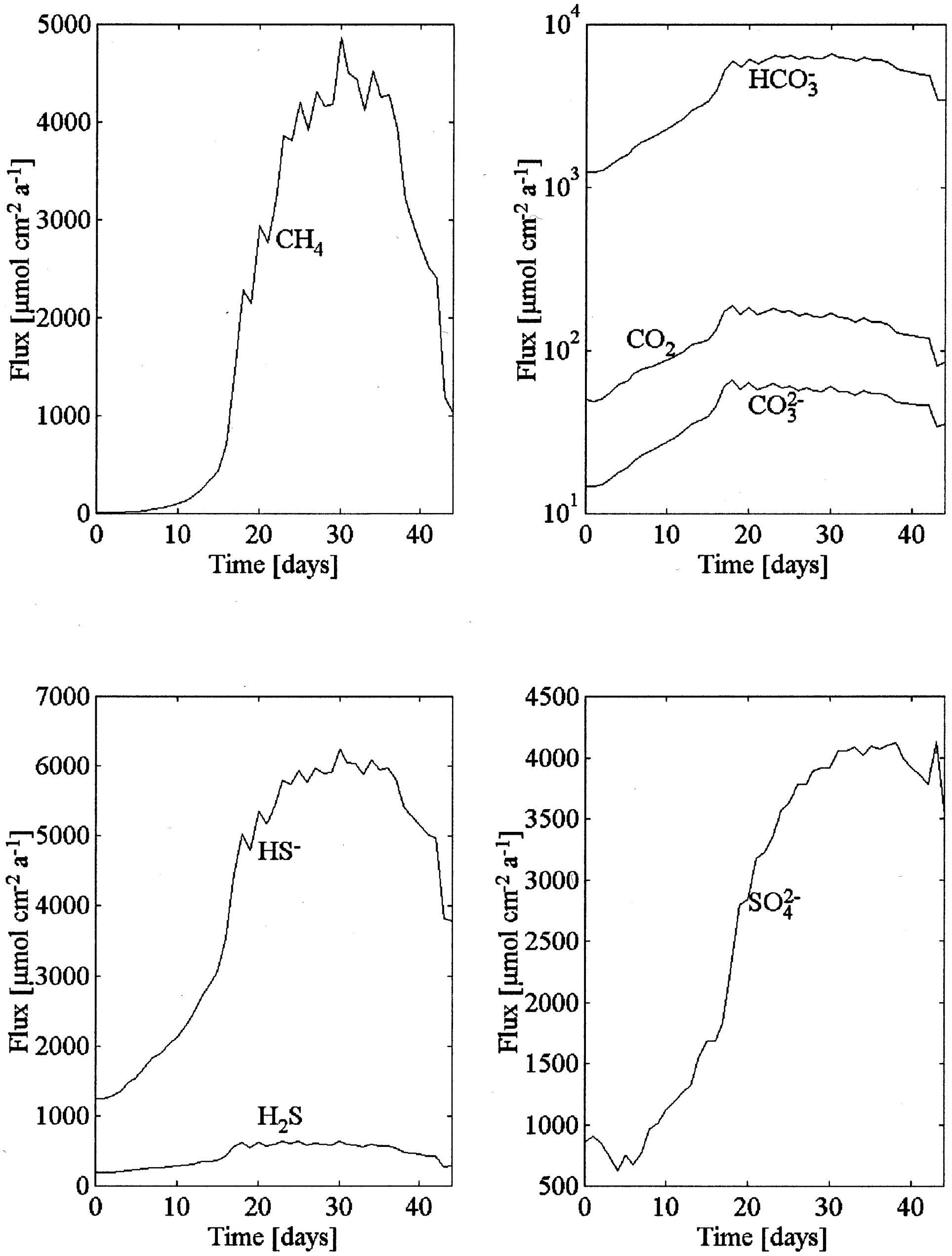

Fig. 5. Fluxes between sediment and overlying bacterial mat (in μmol cm^{-2} a^{-1}) as calculated in the non-steady state simulation forced by the fluid flux rates depicted in Figure 4 (Tryon and Brown, 2001). All fluxes, excluding the SO_4^{2-} flux, are directed out of the sediment.

larger spread of the carbonate precipitation zone. Scenario B differs in the fluid flow velocity, which was set to zero ($v = 0$). The overall rate of carbonate precipitation was decreased by almost 50% upon this manipulation due to the lower rate of methane delivery from below and diminished alkalinity production from anaerobic methane oxidation. The rate constant for methane oxidation (k_{CH4SO4}) had little effect on the precipitation rate as long as the value was larger than 2.5 cm^3 mmol^{-1} a^{-1} (scenarios C, D, E) because in this case methane oxidation was limited by the supply of methane from below. In contrast, a complete shutdown of anaerobic methane oxidation (scenario F, $k_{CH4SO4} = 0$) inhibited carbonate precipitation entirely showing that the carbonate alkalinity generated by methane oxidation is a necessary requirement for carbonate precipitation at this site.

The kinetic constants for aragonite and calcite precipitation were varied to investigate the sensitivity of carbonate precipitation towards the chemical reactions occurring at the mineral surface. These simulations (scenarios G, H, I) clearly show that the precipitation rate is affected by the velocity of surface reactions. Thus, precipitation rates are controlled by both surface reactions and by the rate of alkalinity production from

Table 4. Parameter variations applied the steady state simulations of carbonate precipitation (Fig. 6).

Scenario (Fig. 6)	Velocity [cm a^{-1}]	kCH_4SO_4 [cm^3 $mmol^{-1}$ a^{-1}]	kCALPPT [mmol cm^{-3} a^{-1}]	kARAPPT [mmol cm^{-3} a^{-1}]
A	10	100	10	100
B	0	100	10	100
C	0	10	10	100
D	0	5	10	100
E	0	2.5	10	100
F	0	0	10	100
G	10	100	10	10
H	10	100	1	10
I	10	100	0.1	1

anaerobic methane oxidation. Dissolved Ca is not depleted in the reaction layer (Fig. 2a) demonstrating that the precipitation rate is not limited by Ca delivery from the overlying bottom water at the prevailing rate of fluid flow. Nevertheless, Ca supply from above may become a limiting factor at higher rates of fluid venting.

The sensitivity tests also revealed that aragonite is the dominant authigenic carbonate mineral only at high rates of methane delivery and oxidation ($v \geq 10$ cm a^{-1}, $kCH_4SO_4 \geq 100$ cm^3 $mmol^{-1}$ a^{-1}) and only in the surface area where methane oxidation produces alkalinity. Thus, the occurrence of aragonite precipitates in surface sediments can be taken as a clear indication of strong upward fluid flow and efficient methane oxidation. Moreover, the kinetic constant for aragonite precipitation has to be higher than the corresponding constant for calcite precipitation to obtain the more soluble and less stable mineral (aragonite) as the major precipitation product. When both species (aragonite and calcite) precipitate with the same kinetic constant (scenario G) the aragonite precipitation rate is low because of the stronger oversaturation with respect to the thermodynamically more stable calcite (see Fig. 2a).

In experimental studies of carbonate precipitation from seawater, preferential precipitation of aragonite versus calcite occurs at high temperatures, low dissolved Mg/Ca ratios, high sulfate concentrations and low phosphate levels in the surrounding fluid (Walter, 1986; Burton and Walter, 1987; Morse et al., 1997). The pore fluids contain less sulfate and more phosphate than the overlying seawater and the Mg/Ca ratio of the fluids is enhanced due to carbonate precipitation (Appendix). Nevertheless, the kinetic constant for aragonite precipitation derived from the pore water data is higher than the kinetic constants obtained in laboratory experiments with ordinary seawater (section 5. 1). Thus, the chemical composition of the fluids is probably not responsible for the preferential precipitation of aragonite at Hydrate Ridge. Preferential and rapid formation of aragonite has also been observed at other locations where methane is microbially oxidized under anaerobic conditions (Aloisi et al., 2000). Therefore, it seems to be possible that microbial consortia that oxidize methane anaerobically (Boetius et al., 2000) also catalyze the precipitation of aragonite.

5.4. Biogeochemical Turnover in the Bacterial Mat, Benthic Fluxes and Carbon Budget

The turnover within the *Beggiatoa* sp. mat on the sediment surface as well as the benthic fluxes at the interface between mat and overlying seawater can be calculated using the fluxes at the sediment-mat interface determined in the steady state simulation (Table 5) and applying additional mass balance arguments. It is reasonable to assume that dissolved sulfide flowing out of the sediment is completely oxidized within the mat under the moderate flow conditions applied in the steady-state simulation. Sulfide oxidation by *Beggiatoa* sp. has been studied in detail and it has been shown that these microorganisms can use both dissolved oxygen and nitrate as terminal electron acceptors (Jorgensen and Revsbech, 1983; Sweerts et al., 1990). Moreover, it has to be considered that the chemical energy released in the oxidation reaction is partly invested to produce new bacterial biomass. Sommer et al. (2002) found a CO_2 fixation rate of 182 μmol cm^{-2} a^{-1} in the bacterial mats of Hydrate Ridge. This rate and the sulfide flux determined in the model (1046 μmol cm^{-2} a^{-1}; Table 5) suggest that about 6 mol of sulfide have to be oxidized to produce 1 mol of organic carbon (POC), here presented as carbohydrate $C(H_2O)$. The stoichiometry of the overall reactions may thus be presented as:

$$HS^- + \frac{55}{30}O_2 + \frac{5}{30}CO_2 + \frac{5}{30}H_2O \rightarrow SO_4^{2-} + H^+ + \frac{5}{30}C(H_2O)$$

$$HS^- + \frac{44}{30}NO_3^- + \frac{5}{30}CO_2 + \frac{14}{30}H^+ \rightarrow SO_4^{2-} + \frac{22}{30}N_2 + \frac{17}{30}H_2O + \frac{5}{30}C(H_2O) \quad (6)$$

Dissolved oxygen and nitrate concentrations are similar in the bottom water overlying the sediments of Hydrate Ridge ($\approx$40 μM each). Thus, it may be assumed that both oxidizing agents contribute equally to sulfide oxidation. With this assumption, the benthic oxygen and nitrate fluxes into the bacterial mat due to sulfide oxidation at steady state are 959 μmol O_2 cm^{-2} a^{-1} and 767 μmol NO_3^- cm^{-2} a^{-1}, respectively. These reactions also effect the outflow of carbonate alkalinity ($HCO_3^- + 2\ CO_3^{2-}$) into the overlying bottom water. Considering the rates and stoichiometry derived above and the significant contribution of H_2S to the total sulfide flux (Table 5), protons are produced within the mat at a rate of 400 μmol cm^{-2} a^{-1} so that the flux of carbonate alkalinity from below (862 μmol cm^{-2} a^{-1}) is reduced by almost a factor of two.

Moreover, reactive organic matter is degraded within the

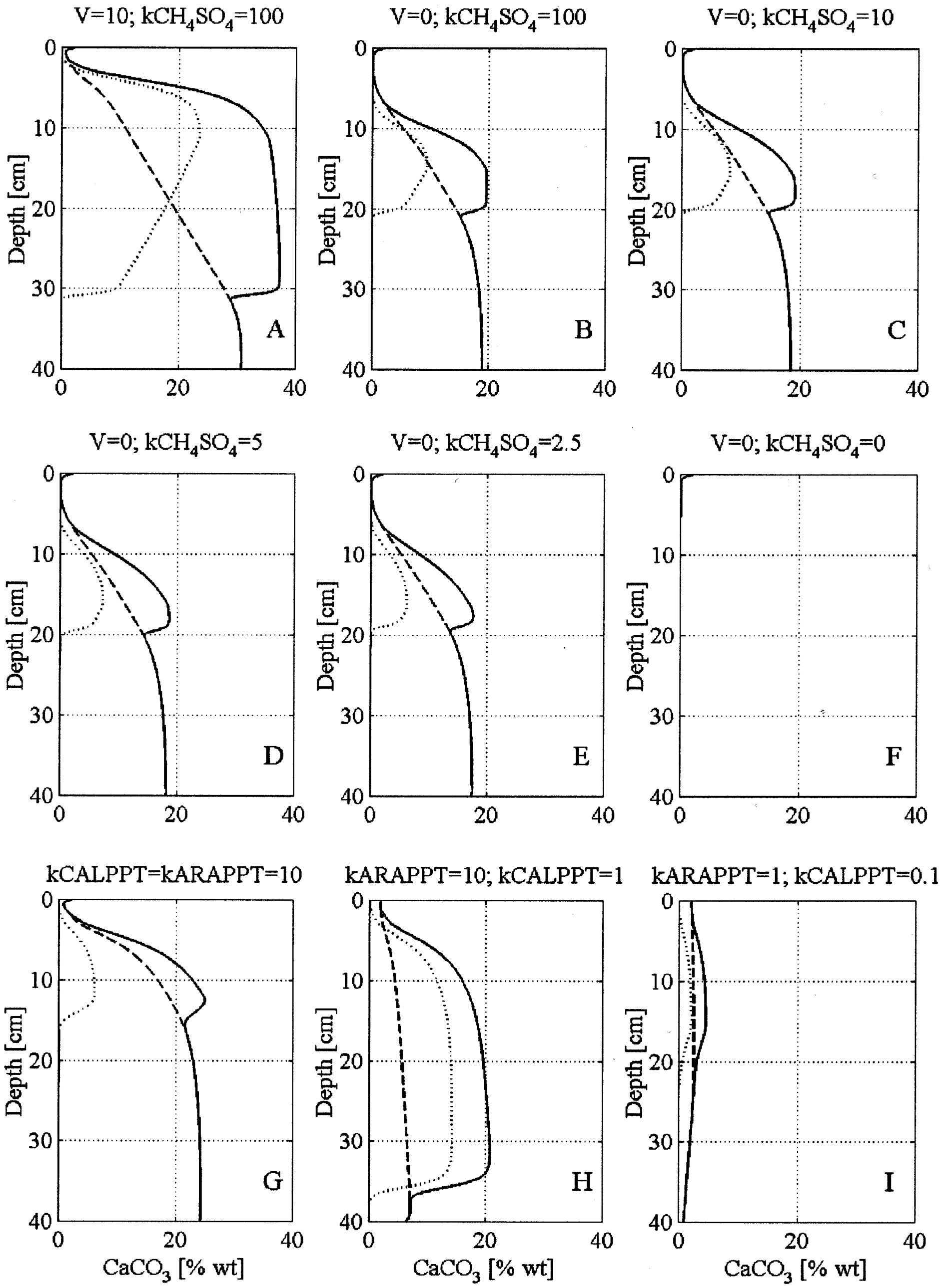

Fig. 6. Sensitivity of carbonate precipitation with respect to fluid flow, methane oxidation and surface processes. Dotted line represents the aragonite, broken line the calcite and the solid line the sum of both i.e., $CaCO_3$ concentration in %wt. The parameter values varied in scenarios A - I are listed in Table 4.

bacterial mat above the sediment surface. The total degradation rate above the mat-sediment interface is calculated to be ≈310 μmol cm^{-2} a^{-1} considering the depositional flux of pelagic POC (≈210 μmol cm^{-2} a^{-1}; Sommer et al., 2002), the authigenic production of POC within the bacterial mat (≈182 μmol cm^{-2} a^{-1}; Sommer et al., 2002), and the POC burial flux at the interface between mat and sediment (81 μmol cm^{-2} a^{-1}; Table 2). Applying a molar ratio between oxygen consumption and POC degradation of 1.4 (Anderson and Sarmiento, 1994) and assuming again that the respiration is equally divided between oxygen consumption and denitrification, the organic matter degradation induces additional oxygen and nitrate fluxes into the bacterial mat of 218 μmol O_2 cm^{-2} a^{-1} and 174 μmol NO_3^- cm^{-2} a^{-1}, respectively. The resulting overall oxygen flux (1177 μmol O_2 cm^{-2} a^{-1}) is rather close to the in-situ oxygen flux at cold vents situated in the eastern Aleutian trench (2890 ± 350 μmol O_2 cm^{-2} a^{-1}; Wallmann et al., 1997).

The data may be further evaluated to produce a comprehensive carbon budget for the investigated site (Fig. 7) using the flux values determined in the numerical simulations (Table 5) and the benthic fluxes derived from stoichiometry and mass balances. Carbon input to the upper sediment column occurs

Table 5. Fluxes of dissolved species at the upper und lower boundary of the model column.

Species	Surface flux [μmol cm^{-2} a^{-1}]	Bottom flux [μmol cm^{-2} a^{-1}]
SO_4^{2-}	896.9	0
TPO4	−0.6	0.03
TNH4	−10.6	1.8
CH_4	−1.4	873.3
Ca	83.6	31.4
CO_2	−48.2	2.5
CO_3^{2-}	−9.3	1.4
HCO_3^-	−843.5	86.3
H_2S	−121.8	28.8
HS^-	−923.8	121.3

Negative signs indicate fluxes out of the sediment.

both from below and from above. The carbon influx at the base of the model column (873 μmol CH_4 cm^{-2} a^{-1} and 89 μmol TCO2 cm^{-2} a^{-1}) and the depositional flux of pelagic matter (210 μmol POC cm^{-2} a^{-1}) yield a total input of 1172 μmol C cm^{-2} a^{-1}. Carbon export also occurs at both ends of the sediment column. At the core base, carbon is buried as authigenic carbonate (120 μmol $CaCO_3$ cm^{-2} a^{-1}) and as particulate organic matter (22 μmol POC cm^{-2} a^{-1}) whereas the remaining carbon is exported as dissolved inorganic carbon into the overlying bottom water (1030 μmol TCO2 cm^{-2} a^{-1}). The methane outflow can be ignored under steady state conditions ($\approx$1 μmol CH_4 cm^{-2} a^{-1}). Overall, a strong influx of CH_4 from deeper sediments constitutes the main source of carbon for the system, while the fluxes of CO_2 and HCO_3^- into the bottom water represent the main carbon output at moderate fluid flow rates.

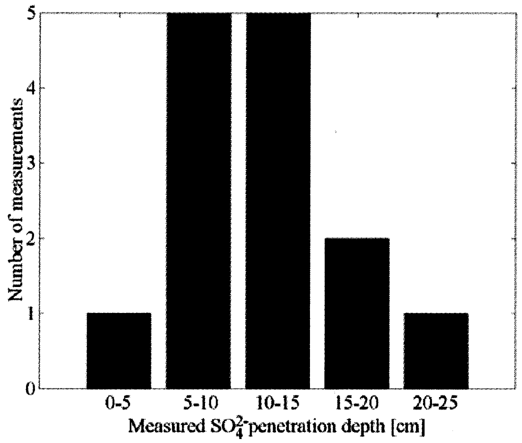

Fig. 8. Measured SO_4^{2-} penetration depths at Hydrate Ridge at stations with clearly visible bacterial mats on the sediment surface. Samples were taken from the northern and southern summits of Hydrate Ridge during two cruises with RV SONNE (SO143 and SO148).

5.5. Spatial Variability of Fluid Flow

The ongoing research at Hydrate Ridge shows that fluid venting is highly variable both in space and in time so that extrapolation of data from only one site may produce misleading results. Thus, the sulfate penetration depths measured at 14 sites at Hydrate Ridge which were covered by bacterial mats (Bohrmann et al., 2000) were used to estimate the variability of fluid venting (Fig. 8). As shown in Figure 4, sulfate penetration is a good indicator for the actual intensity of fluid flow. The model was run repeatedly to explore the sensitivity of the sulfate penetration depth with respect to flow velocity and the depth of the hydrate layer where dissolved methane is assumed to be in equilibrium with gas hydrates (Fig. 9). The velocity of fluid flow was varied between 0 cm a^{-1} and 500 cm a^{-1} with a step size of 1 cm a^{-1} and the depth of the hydrate layer was located between 5 cm and 100 cm below the sediment surface. A total of about 10,000 simulations were run until they reached steady state to determine the sensitivity of the sulfate penetration depth with respect to these model parameters. The other model parameters were set to the values determined previously in the steady state simulation (Tables 1 and 2). The increasing

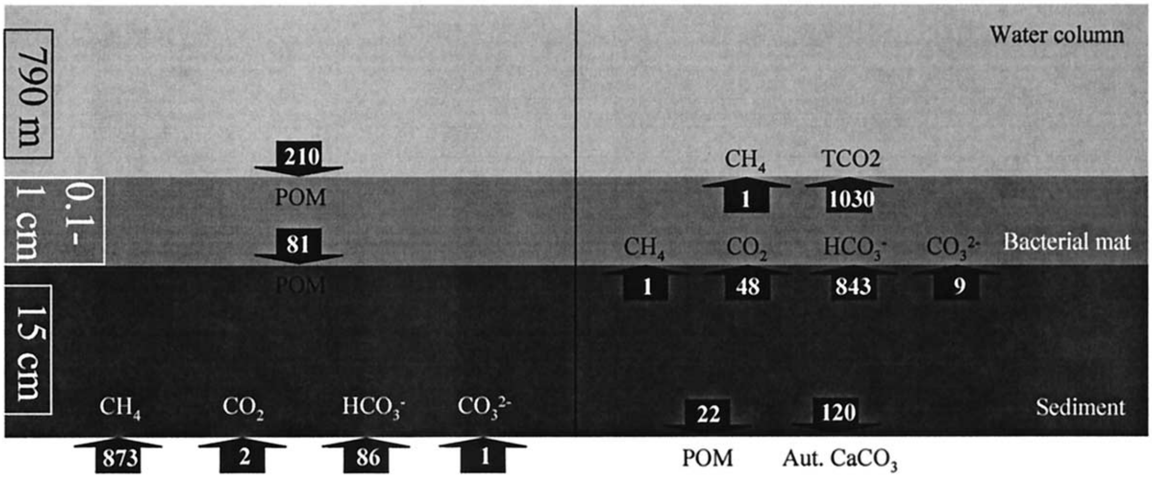

Fig. 7. Carbon budget of the simulated surface sediment (0 - 15 cm) and the overlying bacterial mat. All fluxes are given in μmol cm^{-2} a^{-1}.

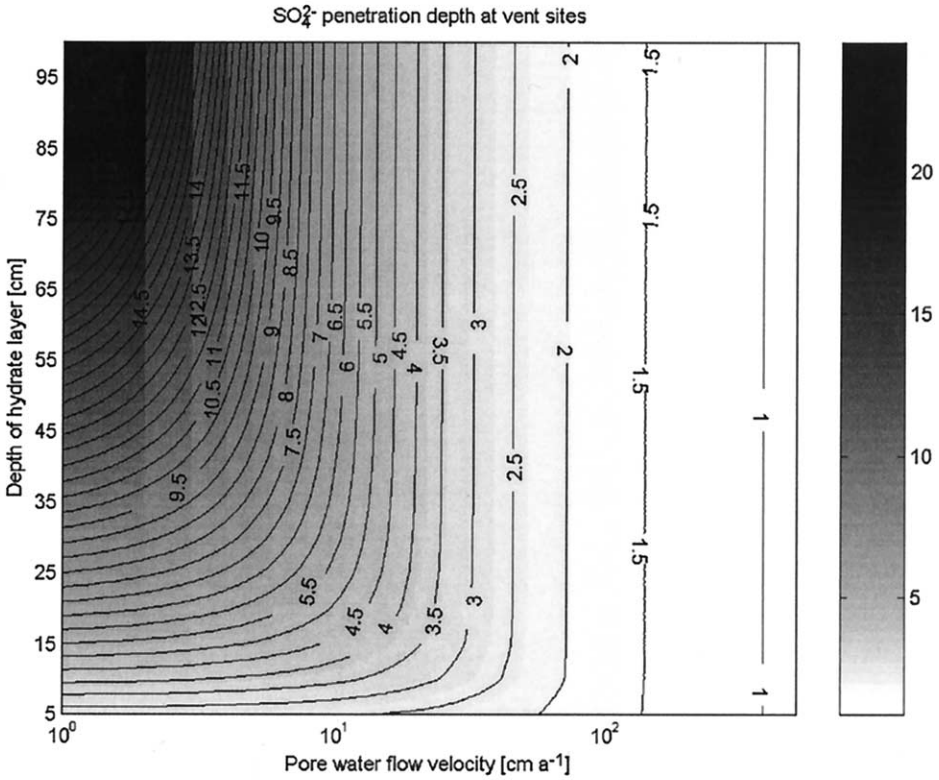

Fig. 9. Sulfate penetration depth (cm) as a function of pore water velocity (cm a^{-1}) and depth of gas hydrate layer (cm), where the gas hydrate is in equilibrium with dissolved methane. The prescribed sulfate concentration at the sediment surface is 27.8 mM (Table 1) whereas the methane concentration at the bottom in equilibrium with gas hydrate amounts to 68 mM at the pressure and temperature conditions prevailing at Hydrate Ridge (Zatsepina and Buffett, 1997).

core length of the simulations requires additional layers to maintain a constant layer thickness of 0.15 mm each.

The simulated sulfate penetration depth as a function of pore water velocity and depth of gas hydrate layer in Figure 9 clearly shows that an increase in advection velocity or a shorter distance between gas hydrates and the sediment surface results in shallower penetration, as expected. This figure also demonstrates that the penetration depth is affected by both parameters for pore water velocities smaller than about 15 cm a^{-1}. Under these conditions molecular diffusion has a significant influence on the species transport so that the penetration depths also depend on the depth of the hydrate layer. The maximum penetration depth of sulfate (24.5 cm) is obtained when advection is zero ($v = 0$) and when the depth of the hydrate layer is set to the maximum value of this sensitivity test (100 cm). For very high pore water velocities (>30 cm a^{-1}) the sulfate penetration depends only on flow velocity.

Using these results, the fluid flow velocity at a particular site can be estimated from the model data if the depths of sulfate penetration and gas hydrate occurrence are known. The histogram depicted in Figure 8 shows that the measured sulfate penetration depths at bacterial mat sites of Hydrate Ridge vary between 0 - 5 cm and 25 cm depth. Hydrates were only recovered from those sediment cores where the sulfate penetration depth was smaller than 10 cm. At the other locations, hydrates were either not present or were located below the core base (20 - 40 cm). The data clearly show that most areas covered with bacterial mats receive less methane from rising fluids than our study site SO143/55-2. They also document a strong lateral variability in sulfate penetration and fluid flow which has to be considered in regional mass balances of methane turnover and benthic carbon cycling.

6. CONCLUSIONS

Our model study confirms that cold vents at convergent margins are affected by a large advective flux of methane from the subsurface, inducing enormous turnover rates in the surface horizons. Moreover these systems are characterized by high spatial and temporal variability in turnover rates as well as species distributions. The simulations clearly depict that biogeochemical measurements can only represent a snapshot of the system, which may be completely different few meters beside or a few days later. Nevertheless, the simulations showed that because of the fast reactions, the pore water composition at this site can be assumed to be in steady state. In other words, the pore water distributions give a good overview of the instantaneously prevailing processes at this local environment. The sulfate penetration depth is a particularly useful parameter which can be used to determine fluid flow rates on a regional scale.

The carbon budget for the simulated sediment column clearly depicts the magnitude of the main carbon sources and sinks for low fluid flow velocities (10 cm a^{-1}). Under these conditions, the flux of dissolved methane from below represents the main source of carbon for the sediment while the main sink is represented by the TCO2 flux through the sediment surface. All other processes (e.g., organic matter degradation or calcium carbonate precipitation/burial) have only a minor impact ($<20\%$) on the total budget. At moderate advective fluxes (<80 cm a^{-1}) the methane from below will be oxidized completely within the sediment. Thus, the outflow of methane into the bottom water can be suppressed almost completely over a broad range of pore water velocities. At higher fluid flow velocities, dissolved methane breaks through the sediment surface into the overlying water column.

Methane is almost completely oxidized by anaerobic microorganisms using dissolved sulfate as electron acceptor at moderate fluid flow rates (0 - 80 cm a^{-1}). Sulfate reduction rates at cold vent sites are typically of the order of 1 mmol cm^{-2} a^{-1}. The global rate of sulfate reduction due to cold venting in subduction zones may be estimated by considering the global water flux in the fore-arc environment induced by sediment compaction (1 - 1.8 km^3 a^{-1}; Wallmann, 2001) and assuming saturation with respect to gas hydrates, which results in dissolved methane concentrations of about 50 - 100 mM CH_4 for the temperature and pressure conditions prevailing at the deep-sea floor (Egeberg and Dickens, 1999). The resulting global rate of sulfate reduction and methane oxidation at cold vent sites (0.05 - 0.18 Tmol a^{-1} with 1 Tmol $= 10^{+12}$ mol) contributes only about 0.1 - 1% to the global rate of sedimentary sulfate reduction in the present ocean (37 Tmol SO_4^{2-} a^{-1}; Canfield, 1993). The importance of cold vents for the deep-sea and continental margin environments becomes more apparent considering that only about 10% of the present sulfate reduction occurs in sediments deposited at water depths of more than 200 m (Middelburg et al., 1993). Moreover, the global rate of methane formation and oxidation in marine sediments seems to be one order of magnitude smaller than the sulfate reduction rate (Canfield, 1993) so that anaerobic methane oxidation at cold vent sites might contribute 1 - 10% to the total methane oxidation in the present ocean.

Enhanced methane concentrations in the water column as well as acoustic plumes above Hydrate Ridge show that methane gas bubbles escape from the sediment producing high methane fluxes (Suess et al., 1999). Our model study suggests that the bubble pathway may be much more efficient than the flow of dissolved methane because bubbles may by-pass the microbial filter located in the surface sediments. Thus, the rise of methane-bearing fluids strongly affects the biogeochemical processes and turnover rates in surface sediments but is of only minor importance for the total methane flux into the water column. Nevertheless, the rise of methane-charged fluids and the dissolution of gas hydrates induce a strong flux of dissolved inorganic carbon into the ocean and a massive loss of oxygen and nitrate from bottom waters due to the oxidation of methane and dissolved sulfide. Thus, our study supports the idea that the large scale dissociation of gas hydrates might affect the oxidation state of seawater and the atmospheric CO_2 contents (Dickens et al., 1995).

A significant fraction of methane-carbon ($\sim 14\%$) is not released into the ocean but precipitated as carbonate mineral due to the anaerobic oxidation of methane. Aragonite is the major carbonate mineral formed upon methane oxidation even though the chemical composition of pore fluids should favor the precipitation of calcite. Thus, it seems to be possible that aragonite formation is induced and catalyzed by microbial processes. Aragonite is dissolved upon burial and is transformed into more stable calcite at depth.

Acknowledgments—The authors like to thank Erwin Suess, who initiated and guided the research at Hydrate Ridge over the past years, for the support and motivation. We also would like to thank Dirk Rickert for collecting and compiling the geochemical data set from Hydrate Ridge during the TECFLUX project and the SO143 and SO148 expeditions, Gerhard Bohrmann for recovering and investigating hydrate and carbonate samples from the Ridge, Michael Tryon for providing his flux rate data set and useful hints, Heiko Sahling for the biologic characterization and classification of vent environments, Stefan Sommer for the investigation of organic carbon fluxes, Peter Linke for the investigation of fluid flow and methane fluxes, Jens Greinert for the detailed map of the location, and Christian Hensen and Matthias Haeckel who helped us with critical discussions of the model results. Moreover, a special thank goes to Bettina Domeyer, Anke Bleyer, and Regina Surberg who analyzed the samples on board of RV SONNE and in the GEOMAR laboratories. We are also grateful for the comments made by the editor Lynn Walter, Dave Archer and two anonymous reviewers. We also thank the Federal Ministry of Research and Technology of Germany for supporting this work within the TECFLUX (grants 03G0143A and 03G0148A), LOTUS (grant 03G0565A), and OMEGA (grant 03G0566A) projects. This is the publication no. 8 of the GEOTECH program and publication no. 25 of the Sonderforschungsbereich 574 “Volatiles and Fluids in Subduction Zones” at Kiel University.

Associate editor: L. Walter

REFERENCES

Aloisi G., Pierre C., Rouchy J.-M., Foucher J.-P., Woodside J., and the MEDINAUT Scientific Party. (2000) Methane-related authigenic carbonates of eastern Mediterranean Sea mud volcanoes and their possible relation to gas hydrate destabilisation. *Earth Planet. Sci. Lett.* **184,** 321–338.

Anderson L. A. and Sarmiento J. L. (1994) Redfield ratios of remineralization determined by nutrient data analysis. *Global Biogeochemical Cycles* **8,** 65–80.

Berner R. A. (1980) *Early Diagenesis - A Theoretical Approach*. Princeton University Press.

Boetius A., Ravenschlag K., Schubert C. J., Rickert D., Widdel F., Gieseke A., Amann R., Jorgensen B. B., Witte U., and Pfannkuche O. (2000) A marine microbial consortium apparently mediating anaerobic oxidation of methane. *Nature* **407,** 623–626.

Bohrmann G., Greinert J., Suess E., and Torres M. (1998) Authigenic carbonates from the Cascadia subduction zone and their relation to gas hydrate stability. *Geology* **26**(7), 647–650.

Bohrmann G., Linke P., Suess E., and Pfannkuche O. (2000) FS SONNE Cruise Report SO143. GEOMAR.

Boudreau B. P. (1996) A method-of-lines code for carbon and nutrient diagenesis in aquatic sediments. *Computers & Geosciences* **22**(5), 479–496.

Burton E. A. and Walter L. M. (1987) Relative precipitation rates of aragonite and Mg calcite from seawater: Temperature or carbonate ion control? *Geology* **15,** 111–114.

Canfield D. E. (1993) Organic matter oxidation in marine sediments. In *Interactions of C, N, P and S Biogeochemical Cycles and Global Change* (ed. R. Wollast, F. T. Mackenzie, and L. Chou), Vol. 14, pp. 333–363, Springer-Verlag.

Dickens G. R., O’Neil J. R., Rea D. K., and Owen R. M. (1995) Dissociation of oceanic methane hydrate as a cause of the carbon isotope excursion at the end of the Paleocene. *Paleoceanography* **10**(6), 965–971.

Egeberg P. K. and Dickens G. R. (1999) Thermodynamics and pore water halogen constraints on gas hydrate distribution at ODP Site 997 (Blake Ridge). *Chem. Geol.* **153,** 53–79.

Egorov A. V., Crane K., Vogt P. R., and Rozhov A. N. (1999) Gas hydrates that outcrop on the sea floor: stability models. *Geo-Marine Letters* **19,** 68–75.

Elvert M., Greinert J., Suess E., and Whiticar M. J. (2001) Carbon isotopes of biomarkers derived from methane-oxidizing microbes at Hydrate Ridge, Cascadia convergent margin. In *Natural Gas Hydrates: Occurrence, Distribution, and Detection,* (ed. C. K. Paull and W. P. Dillon), Vol. 124, pp. 115–129, American Geophysical Union.

Gieskes J. M., Garno T., Brumsack H. (1991) Chemical methods for interstitial water analysis aboard *Joides Resolution* Ocean Drilling Program, Texas A & M University.

Ginsburg G. D., Milkov A. V., Soloviev V. A., Egorov A. V., Cherkashev G. A., Vogt P. R., Crane K., Lorenson T. D., and Khutorskoy M. D. (1999) Gas hydrate accumulation at the Hakon Mosby Mud Volcano. *Geo-Marine Letters* **19,** 57–67.

Ginsburg G. D., Soloviev Cranston R. E., Lorenson T. D., and Kvenvolden K. A. (1993) Gas hydrates from the continental slope, offshore Sakhalin Island, Okhostk Sea. *Geo-Marine Letters* **13,** 41–48.

Given R. K. and Wilkenson B. H. (1985) Kinetic control of morphology, composition, and mineralogy of abiotic sedimentary carbonates. *Journal of Sedimentary Petrology* **55,** 109–119.

Grasshoff K., Ehrhardt M., and Kremling K (1983) *Methods of Seawater Analysis.* Verlag Chemie.

Greinert J., Bohrmann G., and Suess E. (2001) Gas hydrate-associated carbonates and methane-venting at Hydrate Ridge: Classification, distribution, and origin of authigenic lithologies. In *Natural Gas Hydrates - Occurrence, Distribution, and Detection* (ed. C. K. Paull and W. P. Dillon), Vol. 124, pp. 99–113, American Geophysical Union.

Hales B. and Emerson S. (1997) Evidence in support of first-order dissolution kinetics of calcite in seawater. *Earth Planet. Sci. Lett.* **148,** 317–327.

Han M. W. and Suess E. (1989) Subduction-induced pore fluid venting and the formation of authigenic carbonates along the Cascadia continental margin: Implications for the global Ca-cycle. *Palaeogeography, Palaeoclimatology, Palaeoecology* **71,** 97–118.

Hempel P. (1995) Dewatering of sediments along the Cascadia margin: Evidence from geotechnical properties. *Proceedings of the Ocean Drilling Program, Scientific Results.* **146,** 257–274.

Hesselbo S. P., Gröcke D. R., Jenkyns H. C., Bjerrum C. J., Farrimond P., Bell H. S. M., and Green O. R. (2000) Massive dissociation of gas hydrate during a Jurassic oceanic anoxic event. *Nature* **406,** 392–395.

Ivanenkov V. N. and Lyakhin Y. I. (1978) Determination of total alkalinity in seawater. In *Methods of Hydrochemical Investigations in the Ocean* (ed. O. K. Bordovsky and V. N. Ivanenkov), pp. 110–114 (in Russian), Nauka Publ. House.

Iversen N. and Jørgensen B. B. (1985) Anaerobic methane oxidation rates at the sulfate-methane transition in marine sediments from Kattegat and Skagerrak (Denmark). *Limnology and Oceanography* **30**(5), 944–955.

Jacobsen S. B. (2001) Gas hydrates and deglaciations. *Nature* **412,** 691–693.

Jorgensen B. B. and Revsbech N. P. (1983) Colorless sulfur bacteria, Beggiatoa spp. and Thiovulum spp., in O_2 and H_2S microgradients. *Applied and Environmental Microbiology* **45**(4), 1261–1270.

Kulm L. D., Suess E., Moore J. C., Carson B., Lewis B. T., Ritger S. D., Kadko D. C., Thornburg T. M., Embley R. W., Rugh W. D., Massoth G. J., Langseth M. G., Cochrane G. R., and Scamman R. L. (1986) Oregon subduction zone: Venting, fauna, and carbonates. *Science* **231,** 561–566.

Kvenvolden K. A. (1988) Methane hydrates and global climate. *Global Biogeochemical Cycles* **2**(3), 221–229.

Kvenvolden K. A. (1993) Gas hydrates - Geological perspective on global change. *Reviews of Geophysics* **31,** 171–183.

Kvenvolden K. A. (1998) A primer on the geological occurrence of gas hydrate. In *Gas Hydrates: Relevance to World Margin Stability and Climate Change* (ed. J.-P. Henriet and J. Mienert), Vol. 137, pp. 9–30, Geological Society.

Linke P., Suess E., Torres M., Martens V., Rugh W. D., Ziebis W., and Kulm L. D. (1994) In situ measurement of fluid flow from cold seeps at active continental margins. *Deep-Sea Research I* **41**(4), 721–739.

Luff R., Haeckel M., and Wallmann K. (2001) Robust and fast FORTRAN and MATLAB libraries to calculate pH distributions in marine systems. *Computers & Geosciences* **27**(2), 157–169.

Luff R., Wallmann K., Grandel S., and Schlüter M. (2000) Numerical modelling of benthic processes in the deep Arabian Sea. *Deep-Sea Research II* **47**(14), 3039–3072.

Middelburg J. J., Vlug T., and van der Nat F. J. W. A. (1993) Organic matter mineralization in marine systems. *Global and Planetary Change* **8,** 47–58.

Millero F. J. (1995) Thermodynamics of the carbon dioxide system in the oceans. *Geochim. Cosmochim. Acta* **59**(4), 661–677.

Morse J. W., Wang C., and Tsio M. Y. (1997) Influence of temperature and Mg:Ca ratio on $CaCO_3$ precipitates from seawater. *Geology* **25**(1), 85–87.

Raiswell R. (1988) Evidence for surface reaction-controlled growth of carbonate concretions in shales. *Sedimentology* **35,** 571–575.

Sahling H., Rickert D., Lee R. W., Linke P., and Suess E. (2002) Macrofaunal community structure and sulfide flux at gas hydrate deposits from the Cascadia convergent margin, NE Pacific. Marine Ecology Progress Series 231, 121–138.

Sassen R., MacDonald I. R., Guinasso N. L. Jr., Joye S., Requejo A. G., Sweet S. T., Alcala-Herrera J., DeFreitas D. A., and Schink D. R. (1998) Bacterial methane oxidation in sea-floor gas hydrate: Significance to life in extreme environments. *Geology* **26**(9), 851–854.

Sassen R., Sweet S. T., Milkov A. V., DeFreitas D. A., and Kennicutt II M. C. (2001) Thermogenic vent gas and gas hydrate in the Gulf of Mexico slope: Is gas hydrate decomposition significant? *Geology* **29**(2), 107–110.

Sommer S., Pfannkuche O., Rickert D., and Kähler A. (2002) Ecological implications of surficial marine gas hydrates for the associated small-sized benthic biota at the Hydrate Ridge (Cascadia Convergent Margin, NE Pacific). *Marine Ecology Progress Series* **243,** 25–38.

Suess E., Carson B., Ritger S. D., Moore J. C., Jones M. L., Kulm L. D., and Cochrane G. R. (1985) Biological communities at vent sites along the subduction zone off Oregon. In *The Hydrothermal Vents of the Eastern Pacific: An Overview* (ed. M. L. Jones), Vol. 6, pp. 475–484, Bull. Biol. Soc. Wash.

Suess E., Torres M., Bohrmann G., Collier R. W., Greinert J., Linke P., Rheder G., Trehu A., Wallmann K., Winckler G., and Zuleger E. (1999) Gas hydrate destabilization: Enhanced dewatering, benthic material turnover and large methane plumes at the Cascadia convergent margin. *Earth Planet. Sci. Lett.* **170,** 1–15.

Sweerts J.-P. R. A., DeBeer D., Nielsen L. P., Verdouw H., Heuvel J. C. V. D., Cohen Y., and Cappenberg T. C. (1990) Denitrification by sulphur oxidizing Beggiatoa spp. mats on freshwater sediments. *Nature* **344,** 762–763.

Tryon M. D. and Brown K. M. (2001) Complex flow patterns through Hydrate Ridge and their impact on seep biota. *Geophysical Research Letters* **28**(14), 2863–2867.

Tryon M. D., Brown K. M., Torres M. E., Tréhu A. M., McManus J., and Collier R. W. (1999) Measurements of transience and downward fluid flow near episodic methane gas vents, Hydrate Ridge, Cascadia. *Geology* **27**(12), 1075–1078.

Van Cappellen P. and Wang Y. (1996) Cycling of iron and manganese in surface sediments: A general theory for the coupled transport and reaction of carbon, oxygen, nitrogen, sulfur, iron, and manganese. *American Journal of Science* **296,** 197–243.

Wallmann K. (2001) The geological water cycle and the evolution of marine $\delta^{18}O$ values. *Geochim. Cosmochim. Acta* **65**(15), 2469–2485.

Wallmann K., Linke P., Suess E., Bohrmann G., Sahling H., Schlüter M., Dählmann A., Lammers S., Greinert J., and von Mirbach N. (1997) Quantifying fluid flow, solute mixing, and biogeochemical turnover at cold vents of the eastern Aleutian subduction zone. *Geochim. Cosmochim. Acta* **61**(24), 5209–5219.

Walter L. M. (1986) Relative efficiency of carbonate dissolution and precipitation during diagenesis: A progress report on the role of solution chemistry. In *Roles of Organic Matter in Mineral Diagenesis* (ed. D. L. Gautier), Vol. 38, pp. 1–12. Society of Economic Paleontologists and Mineralogists, Tulsa.

Wilkenson M. (1989) Evidence for surface reaction-controlled growth of carbonate concretions in shales. *Sedimentology* **36,** 951–953.

Zatsepina O. Y. and Buffett B. A. (1997) Phase equilibrium of gas hydrate: Implications for the formation of hydrate in the deep-sea floor. *Geophysical Research Letters* **24**(13), 1567–1570.

Zhong S. and Mucci A. (1993) Calcite precipitation in seawater using a constant addition technique: A new overall reaction kinetic expression. *Geochim. Cosmochim. Acta* **57,** 1409–1417.

APPENDIX

Complete set of parameters measured at the investigated station (SO143/55-2; 44°34.15′ N; 125°08.73′ W, see Fig. 1). Upper table: Pore water data. Lower table: Solid phase concentrations.

depth [cm]	SiO_2 [μM]	PO_4 [μM]	NO_3 [μM]	NH_4 [μM]	TA [mM]	pH	Cl [mM]	SO_4 [mM]	H_2S [mM]	Mg [mM]	Ca [mM]	Mn [μM]	B [mM]
0.5	230	47.3	0.00	117	15.9	7.88	545	15.8	7.15	52.1	6.99	0.18	0.388
1.5	252	28.8	0.00	133	21.4	8.21	547	7.00	9.15	50.9	5.70	0.14	0.376
2.5	264	55.4	0.00	171	25.3	8.33	543	8.18	13.3	50.9	5.21	0.22	0.390
3.5	267	26.1	0.00	167	28.4	8.17	545	2.20	15.2	50.3	4.42	0.10	0.380
4.5	259	23.1	0.00	182	29.4	8.20	548	2.85	16.7	50.5	4.34	0.18	0.380
5.5	255	30.7	0.00	191	29.3	8.18	546	2.20	15.5	50.1	4.34	0.14	0.378
6.5	221	14.4	0.00	185	30.9	8.55	546	1.95	18.9	50.5	4.00	0.12	0.368
7.5	245	20.1	0.00	182	31.2	8.66	547	2.30	18.4	50.5	3.98	0.12	0.368
8.5	259	26.1	0.00	204	30.7	8.38	547	1.80	16.3	50.7	3.94	0.16	0.368
9.5	252	19.7	0.00	213	30.8	8.48	547	1.75	17.8	49.1	3.98	0.16	0.366
11.5	272	12.9	0.00	222	31.4	7.94	551	1.90	20.1	49.9	3.96	0.20	0.376
14.5	252	11.7	0.00	208	30.8	8.04	541	2.60	20.9	49.1	3.84	0.20	0.354

depth [cm]	C_{org} [%wt]	N [%wt]	S [%wt]	$CaCO_3$ [%wt]	Fe [mg/g]	Mn [mg/g]
0.5	1.63	0.268	1.73	8.69	50.5	0.439
1.5	1.28	0.206	1.36	24.1	44.2	0.386
2.5	1.31	0.211	1.40	22.0	44.8	0.398
3.5	1.34	0.208	1.44	16.7	48.8	0.424
4.5	1.33	0.201	1.37	15.2	46.7	0.419
5.5	1.38	0.206	1.31	13.4	49.9	0.418
6.5	1.31	0.174	0.84	10.7	48.9	0.463
7.5	1.28	0.183	0.95	11.0	49.5	0.475
8.5	1.33	0.179	1.13	11.3	48.4	0.449
9.5	1.44	0.195	1.26	14.3	46.3	0.415
11.5	1.34	0.201	1.28	14.1	44.8	0.404
14.5	1.23	0.173	1.04	19.4	44.1	0.405